

# Slow-growth approximation for near-wall patch representation of wall-bounded turbulence

Sean P. Carney<sup>1</sup> and Robert D. Moser<sup>2,3†</sup>

<sup>1</sup>Department of Mathematics, University of California, Los Angeles, CA 90095, USA

<sup>2</sup>Oden Institute for Computational Engineering and Sciences, The University of Texas at Austin, TX 78712, USA

<sup>3</sup>Department of Mechanical Engineering, The University of Texas at Austin, TX 78712, USA

(Received xx; revised xx; accepted xx)

Wall-bounded turbulent shear flows are known to exhibit universal small-scale dynamics that are modulated by large-scale flow structures. Strong pressure gradients complicate this characterization, however; they can cause significant variation of the mean flow in the streamwise direction. For such situations, we perform asymptotic analysis of the Navier-Stokes equations to inform a model for the effect of mean flow growth on near-wall turbulence in a small domain localized to the boundary. The asymptotics are valid whenever the viscous length scale is small relative to the length scale over which the mean flow varies. To ensure the correct momentum environment, a dynamic procedure is introduced that accounts for the additional sources of mean momentum flux through the upper domain boundary arising from the asymptotic terms. Comparisons of the model's low-order, single-point statistics with those from direct numerical simulation and well-resolved large eddy simulation of adverse-pressure gradient turbulent boundary layers indicate the asymptotic model successfully accounts for the effect of boundary layer growth on the small-scale near-wall turbulence.

**Key words:**

## 1. Introduction

High Reynolds number wall-bounded turbulent shear flows are characterized by a separation of scales between the flow in the near-wall region, in which mean viscous stresses play an important role, and the flow farther away from the wall, where mean viscous effects are negligible. The friction Reynolds number  $Re_\tau = \delta/\delta_\nu$  quantifies this separation of scales, where  $\delta$  is the characteristic length scale of the shear layer, such as a channel half-width, a pipe radius, or a boundary layer thickness, and  $\delta_\nu = \nu/u_\tau$  is the viscous length scale, where  $\nu$  is the kinematic viscosity of the fluid,  $u_\tau = \sqrt{\tau_w/\rho}$ ,  $\tau_w$  is the mean wall shear stress, and  $\rho$  is the fluid density. To simulate all the scales of motion in a wall bounded flow requires  $\mathcal{O}(Re_\tau^{2.5})$  and  $\mathcal{O}(Re_\tau^2)$  spatial degrees of freedom for direct numerical simulation (DNS) and large eddy simulation (LES), respectively (Mizuno & Jiménez 2013). Even on modern high-performance computing systems, this cost is prohibitively large for important atmospheric and aeronautical flows, for example, which

† Email address for correspondence: rmoser@oden.utexas.edu

routinely occur at  $10^4 \lesssim Re_\tau \lesssim 10^7$ , (Smits & Marusic 2013). Developing reduced order models, such as wall-modeled LES, to overcome this challenge requires an understanding of the mutual interactions between small and large-scale motions in the outer and near-wall regions.

Advances in computational power and experimental techniques have enabled a great deal of insight into the inner/outer interactions for the canonical zero-pressure gradient boundary layer and fully developed pipe and channel flows (Smits *et al.* 2011). It is well established that there is an autonomous near-wall cycle of self sustaining mechanisms (Jiménez & Moin 1991; Hamilton *et al.* 1995; Jeong *et al.* 1997), involving low and high speed streamwise velocity streaks and coherent structures of quasi-streamwise vorticity. Jiménez & Pinelli (1999) showed that this cycle of near-wall dynamics persists without any input from the turbulence farther away from the wall. Large-scale motions, or superstructures, in the outer layer do indeed impact the near-wall region, however. They modulate the turbulent velocity fluctuations and superimpose their energy (Hutchins & Marusic 2007; Marusic *et al.* 2010a; Ganapathisubramani *et al.* 2012), and their influence increases with  $Re_\tau$  (DeGraaff & Eaton 2000). Spectral analysis of both channel (Lee & Moser 2019; Wang *et al.* 2021) and boundary layer flow data (Samie *et al.* 2018) has demonstrated that, in contrast, the dynamics of the small-scale motions in the near-wall region are universal. The small-scale, high-wavenumber energy, as well as its production, dissipation, and transport, are independent of  $Re_\tau$ .

Based on this characterization of near-wall dynamics, Carney *et al.* (2020) formulated numerical simulations on near-wall ‘patch’ (NWP) domains whose size scaled in viscous units. Similar to the numerical experiments of Jiménez & Moin (1991) and Jiménez & Pinelli (1999), the model used restricted domain sizes and, as in the latter, manipulation of the turbulence outside of the near-wall region to simulate *only* the autonomous dynamics over the range of scales at which they occur. The model reproduced near-wall small-scale statistics obtained from direct numerical simulation, confirming that the ‘universal signal’ described in Marusic *et al.* (2010b); Mathis *et al.* (2011) indeed arises from universal dynamics, independent of  $Re_\tau$  or external flow configuration. As a computational model, the near-wall patch (NWP) defined a one parameter family of turbulent flows parameterized by the near-wall, viscous-scaled pressure gradient. Because of its ability to reproduce a variety of well-known features of high  $Re_\tau$  wall turbulence at a computational cost that is orders of magnitude less than DNS, the model offers a way to efficiently probe the response of near-wall turbulence to changes in the mean momentum environment.

The NWP model was validated against DNS data from channel flows, featuring mild favorable-pressure gradients, and a zero-pressure gradient (ZPG) boundary layer. Because of their relevance to engineering applications, it is reasonable to ask if the NWP model can adequately describe the near-wall, small-scale dynamics of flows with adverse-pressure gradients (APGs), especially APG boundary layers. Although the understanding of scale interactions between inner and outer regions in APG boundary layers is less complete than for ZPG flows, there has been much progress since the early experimental studies of Clauser (1954) and Bradshaw (1967) and numerical simulations of Spalart & Leonard (1987) and Spalart & Watmuff (1993); see also references therein. More recent experimental investigations include Rahgozar & Maciel (2012), Harun *et al.* (2013), Knopp *et al.* (2015), Knopp *et al.* (2017), Sanmiguel Vila *et al.* (2017, 2020) and Romero *et al.* (2022). Previous large-scale simulations include DNS (Na & Moin 1998; Skote & Henningson 2002; Gungor *et al.* 2016) and well-resolved LES (Hickel & Adams 2008) of separated boundary flows and a separated channel flow (Marquillie *et al.* 2008), while large scale simulations of attached APG boundary layers have been conducted by Lee

& Sung (2009); Kitsios *et al.* (2017); Lee (2017); Yoon *et al.* (2018) using DNS, as well as by Inoue *et al.* (2013); Bobke *et al.* (2017); Pozuelo *et al.* (2022) using well-resolved LES. Simulations over complex airfoil geometries have also been performed with both DNS (Hosseini *et al.* 2016) and well-resolved LES (Sato *et al.* 2017; Tanarro *et al.* 2020).

One observation that has consistently emerged in the literature is that, even when mild, adverse pressure gradients energize the large-scale structures in both the outer layer and the near-wall region of the the boundary layer. The increased influence of the large-scales also results in increased modulation effects on the small-scale APGs (Harun *et al.* 2013; Lee 2017; Yoon *et al.* 2018), analogous to the effect of increasing  $Re_\tau$  in ZPG boundary layers. Although APGs have been shown to energize the small-scale motions in the outer region of a boundary layer (Sanmiguel Vila *et al.* 2020), less appears to be known about the small-scale energy in the near-wall region. After filtering out contributions from spanwise wavelengths  $\lambda_z/\delta_\nu \gtrsim 180$ , Lee (2017) found the small-scale contribution to both the streamwise velocity variance and the Reynolds shear stress increased with pressure gradient, while Sanmiguel Vila *et al.* (2020) found that the small-scale contributions to the streamwise velocity variance from motions with streamwise wavelengths  $\lambda_x/\delta_\nu \lesssim 4300$  was independent of the pressure gradient strength. One objective of the current work is to use a near-wall patch computational model to investigate the extent to which the small-scale, near-wall dynamics are responsible for the observed statistical properties of adverse-pressure gradient flows. Since the NWP model simulates only the small-scales motions, isolated from large-scale influences, any differences between its statistical profiles and those from DNS or large-scale simulations can reasonably be attributed to the superposition and modulation effects of the large-scale motions that are missing.

The near-wall patch model previously developed in Carney *et al.* (2020) can be considered the lowest order asymptotic description of small-scale, near-wall dynamics in which the mean pressure gradient, the momentum flux from the outer flow, and the mean wall shear stress are all uniform in time and space on the scale of the computational domain. To account for the relatively rapid downstream development of mean quantities in adverse-pressure gradient boundary layers (Kitsios *et al.* 2017), we develop in the present work a higher-order approximation that allows the mean wall shear stress to develop slowly in the streamwise direction. Similar to Spalart (1988); Guarini *et al.* (2000); Maeder *et al.* (2001) and Topalian *et al.* (2017), asymptotic analysis is used to derive a set of ‘homogenized’ equations that describe the mean effect of streamwise development on the near-wall dynamics.

If such a higher order computational model can be shown to accurately reproduce the near-wall, small-scale features of adverse-pressure gradient flows, or, more generally, for flows that feature asymptotic growth of mean quantities in the near-wall region, it could be used to inform a pressure-gradient dependent wall model for LES Piomelli & Balaras (2002); Bose & Park (2018). In this setting, the model is a pressure-gradient-dependent analogue to the experimentally determined ‘universal signal’ of Mathis *et al.* (2011). A time-dependent sequence of model flow fields could also potentially be used to generate a statistical ensemble that could then train a deep neural network approach to wall-modeling, as in Yang *et al.* (2019). Additionally, the model could be used to study the interaction between small-scale near-wall turbulent dynamics and more complicated physical processes such as heat transfer, chemical reactions, turbophoresis, or surface roughness.

The rest of the paper is organized as follows: §2 contains a description of the computational model and the numerical method used to integrate the equations of motion. Section 3 provides a comparison between the statistics generated by the model and

the corresponding quantities from DNS for the cases of both zero and mild adverse pressure gradients. In section 4 the results are summarized, and possible applications and extensions of the model are discussed.

### 1.1. Mathematical notation and nomenclature

In the following discussion, the velocity components in the streamwise ( $x$ ), wall-normal ( $y$ ) and spanwise ( $z$ ) directions are denoted as  $u$ ,  $v$ , and  $w$ , respectively, and when using index notation, these directions are labeled 1, 2, and 3, respectively. The expected value is denoted with angle brackets (as in  $\langle \cdot \rangle$ ), and upper case  $U$  and  $P$  indicate the mean velocity and pressure, so that  $\langle u_i \rangle = U_i$ . The velocity and pressure fluctuations are indicated with primes, e.g.  $u_i = U_i + u'_i$ . Partial derivatives shortened to  $\partial_i$  signify  $\partial/\partial x_i$ , differentiation in the direction  $x_i$ . The mean advective derivative is  $D(\cdot)/Dt = \partial_t(\cdot) + U_j \partial_j(\cdot)$ , where Einstein summation notation is implied. In general, repeated indices imply summation, with the exception of repeated Greek indices. Lastly, the superscript ‘+’ denotes non-dimensionalisation with the kinematic viscosity  $\nu$  and the friction velocity  $u_\tau$ .

## 2. Motivation

### 2.1. Fundamental modeling assumptions

Intrinsic to the computational model is the assumption of a separation of temporal and spatial scales between the small-scale turbulence arising from the autonomous near-wall dynamics and the large-scale outer-layer turbulence. The near-wall dynamics are thus considered to be in local equilibrium with both the pressure gradient and momentum flux environment in which they evolve. In the previous near-wall patch formulation (Carney *et al.* 2020), it was further assumed these quantities were uniform in space and time on the scale of the dynamics being simulated. In the current work, however, the local mean wall shear stress is allowed to vary slowly in the streamwise direction, which should allow for a higher order asymptotic description of near-wall turbulence than before. With these assumptions, the near-wall model will be representative of a variety of flows that are not in equilibrium overall, including those with non-constant pressure gradients. However, the modeling approach breaks down, for example, for a boundary layer near separation.

### 2.2. Growth effects in the near-wall region of turbulent boundary layers

Consider a flat plate turbulent boundary layer that is homogeneous in the spanwise direction and under the influence of a pressure gradient in the streamwise direction. Let the pressure gradient be parameterized by

$$\beta = \frac{\delta}{\tau_w} \frac{dP_\infty}{dx}, \quad (2.1)$$

which is the standard nondimensional Clauser parameter, where  $\delta$  is the boundary layer displacement thickness,  $\tau_w$  is the mean shear stress at the wall, and  $dP_\infty/dx$  is the far-field pressure gradient with a unit density. For any  $\beta \in [0, \infty)$  the boundary layer as a whole will grow in the streamwise direction; a fortiori, so too will the near-wall region. Below we make two observations about the effect this growth has on the near-wall region of turbulent boundary layers (TBLs). These observations motivate the multiscale asymptotic analysis that will inform the slow-growth near-wall patch model.

The first observation is that the near-wall region of TBLs grows more rapidly with increasing  $\beta$ . As  $\tau_w$  evolves downstream, so too does the viscous length scale characterizing the local near-wall scaling. Figure 1 illustrates the streamwise evolution of the

---

Large scale simulation	$Re_\tau$	$\beta$	$dP^+/dx^+$	$\epsilon$
SJM2000	1989.4	0	0	$-2.985 \cdot 10^{-7}$
KS- $\beta 1$	184.6	1.02	$5.503 \cdot 10^{-3}$	$-9.4303 \cdot 10^{-6}$
BVOS- $\beta 1.7$	760.1	1.72	$8.981 \cdot 10^{-3}$	$-1.064 \cdot 10^{-5}$

---

Table 1: Parameters from the large-scale simulations considered at the streamwise location marked ‘ $\times$ ’ in figure 1.

friction velocity  $u_\tau$  for the three large-scale simulation cases considered throughout this work, namely SJM- $\beta 0$  (Sillero *et al.* 2013), KS- $\beta 1$  (Kitsios *et al.* 2017) and BVOS- $\beta 1.7$  (Bobke *et al.* 2017), labeled by the value of the Clauser parameter (2.1) at the streamwise locations marked in each case by ‘ $\times$ ’ in the figure. Each friction velocity and streamwise location is scaled by the kinematic viscosity and value of  $u_\tau$  at these particular locations, denoted below by  $\bar{x}$ . For SJM- $\beta 0$ ,  $\bar{x}$  is selected as the location with the largest value of  $Re_\tau$  for which statistical profiles are reported, while  $\bar{x}$  is selected for the BVOS- $\beta 1.7$  case to maximize  $Re_\tau$  before boundary effects from the ‘fringe region’ used to periodically match the TBL inlet and outlet profiles (Bobke *et al.* 2017) affect the statistics (this region corresponds to the locations in figure 1(c) where  $\partial u_\tau / \partial x$  is positive). Since both  $\beta$  and  $Re_\tau$  are approximately constant throughout the domain for the KS- $\beta 1$  simulation,  $\bar{x}$  is simply taken in the middle.

The rate of change of the friction velocity with respect to streamwise position  $x$  can be used to define a length scale  $L$  that quantifies the streamwise distance over which the near-wall region grows. Define  $L$  by

$$L^{-1} = \frac{1}{u_\tau} \frac{\partial u_\tau}{\partial x} \quad (2.2)$$

where both  $u_\tau$  and  $\partial u_\tau / \partial x$  are evaluated at  $\bar{x}$ . Using also the viscous length scale  $l_\nu$  at  $\bar{x}$ , define the nondimensional asymptotic parameter

$$\epsilon = \frac{l_\nu}{L} = \frac{\nu}{u_\tau^2} \frac{\partial u_\tau}{\partial x}. \quad (2.3)$$

The value of  $\epsilon$  for each TBL case shown in figure 1 ranges from approximately  $10^{-5}$  to  $10^{-7}$ , as listed in table 1. For SJM- $\beta 0$  and KS- $\beta 1$ , the derivative  $\partial u_\tau / \partial x$  is estimated by differentiating a quadratic and linear least-squares approximation to  $u_\tau$ , respectively. The  $u_\tau$  data is relatively noisy in the BVOS case, so the data is first filtered with a Savitzky-Golay filter (Savitzky & Golay 1964), and it is then separately fit to a piecewise cubic spline interpolant. The derivative  $\partial u_\tau / \partial x$  is then taken to be the average of the derivatives of these two approximations.

The dimensionless parameter  $\epsilon$  is readily seen to be the (negative) streamwise rate of change of the viscous length scale, and it can also be taken as the inverse Reynolds number based on  $L$  and  $u_\tau$ :

$$Re_\epsilon = L/l_\nu.$$

The asymptotic analysis detailed in Section 2.3 is then valid for asymptotically large  $Re_\epsilon$ ; the infinite  $Re_\epsilon$  limit corresponds to zero-growth of the near-wall layer, e.g. in a channel or pipe flow, while the vanishing  $Re_\epsilon$  limit corresponds to boundary layer separation.

The second observation about growth effects in the near-wall region of TBLs is that there is an increase in momentum flux towards the wall with increasing  $\beta$ ; in particular,

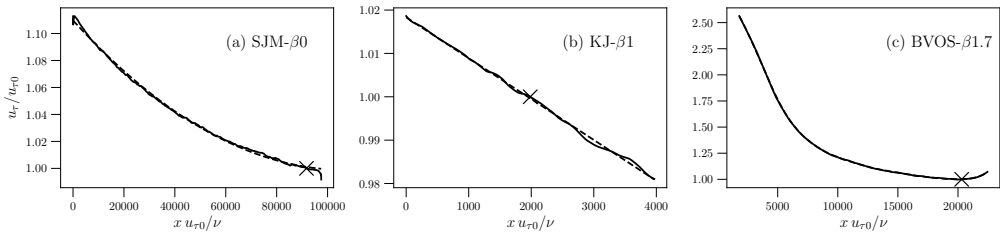


Figure 1: Friction velocity  $u_\tau/u_{\tau 0}$  versus streamwise location  $x u_{\tau 0}/\nu$  for each case in table 1, where  $u_{\tau 0}$  is the value of the friction velocity at the locations marked ‘x’. The dashed lines in (a) and (b) show quadratic and linear least-squares approximations, respectively, while in (c) they show a piecewise cubic least-squares fit.

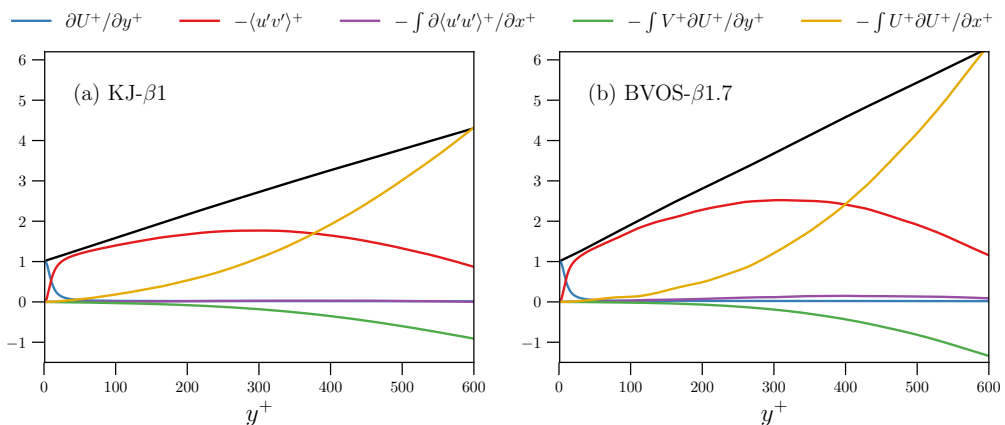


Figure 2: Contributions to the total stress (2.4) versus  $y^+$  for the KS- $\beta 1$  case (a) and BVOS- $\beta 1.7$  case (b). The black curves show the sum of all contributions, i.e. the right-hand side of (2.4).

the Reynolds shear stress increases in magnitude. To quantify this, consider the mean stress balance in viscous units for a TBL with (locally) constant pressure gradient  $dP/dx$ :

$$1 + \frac{dP^+}{dx^+} y^+ = \frac{\partial U^+}{\partial y^+} - \langle u'v' \rangle^+ + \int_0^{y^+} \left( U^+ \frac{\partial U^+}{\partial x^+} + V^+ \frac{\partial U^+}{\partial s^+} + \frac{\partial}{\partial x^+} \langle u'u' \rangle^+ - \frac{\partial^2 U^+}{\partial x^+ \partial x^+} \right) ds. \quad (2.4)$$

Note that here  $s$  is just a dummy variable of integration. As  $dP^+/dx^+$  increases, so too must the mean total stress on the right hand side of (2.4). Figure 2 illustrates this balance for the two mild adverse-pressure-gradient TBL flows KS- $\beta 1$  and BVOS- $\beta 1.7$ , where, as before, quantities are scaled in viscous units at the locations marked ‘x’ in figure 1. Besides the Reynolds shear stress, the mean convective terms make a significant contribution to the stress balance, even in the near-wall region  $y^+ \leq 300$ . In contrast, the mean convective terms from SJM- $\beta 0$  make a negligible contribution to the overall stress balance (not shown). In all cases, the mean viscous and turbulent fluctuation growth terms in (2.4) do not make a meaningful contribution to the total stress balance.

Large-scale numerical simulation of turbulent boundary layers properly account for

the effect of boundary layer growth on the near-wall region simply by computing on domains that are sufficiently large. Clever ‘recycling’ and rescaling techniques Lund *et al.* (1998); Colonius (2004); Araya *et al.* (2011); Sillero *et al.* (2013) are typically used to increase size of the part of the domain containing “healthy” turbulence (i.e. turbulence not impacted by inflow-outflow artifacts) while ensuring the simulations remain computationally affordable. Spalart (1988), however, took an alternative approach to achieve this goal. Assuming a scale separation between the size of the boundary layer and the streamwise length over which it develops, asymptotic analysis was used to determine a set of ‘homogenized’ equations of motion featuring the standard Navier-Stokes equations augmented with additional terms modeling the effect of boundary layer growth.

Inspired by the approach in Spalart (1988), we now describe a multiscale analysis to build a near-wall patch representation of the near-wall, small-scale dynamics of turbulent flows with asymptotically small  $\epsilon$ . In this case the separation of scales assumed in Spalart (1988) is expected to be even stronger, since only the near-wall layer is of interest, in contrast to the entire boundary layer.

### 2.3. Multiscale asymptotic analysis

The goal of the following analysis is to derive a set of equations for a near-wall patch domain that can produce accurate near-wall statistics for spatially developing flows.

First, if the viscous length scale evolves over distances that are asymptotically large relative to its local values, it is sensible to hypothesize a scaling relationship for the fluid velocity of the form

$$u_i(x, y, z) = u_\tau(\epsilon x^+) u_i^+(x^+, y^+, z^+), \quad (2.5)$$

where  $\epsilon$  is the dimensionless order parameter (2.3) and  $u_i^+$  is considered statistically homogeneous in the stream and spanwise directions. This homogeneity will allow for the use of periodic boundary conditions (and Fourier spectral discretizations) for the near-wall patch domain, as in Spalart (1988). The superscript ‘+’ here denotes nondimensionalization by the local viscous scale. Equation (2.5) is nothing but the standard near-wall viscous scaling where the friction velocity evolves slowly in the streamwise direction.

For some specific streamwise location  $\bar{x}$ , let

$$\bar{l}_\nu := l_\nu \Big|_{x=\bar{x}}$$

denote the local viscous length scale, and let  $L$  be the length scale defined by (2.2); that is, the inverse of the logarithmic derivative of  $u_\tau$ . For some given  $\epsilon$ , define  $X = \epsilon x$ , as well as the new coordinates

$$(x, y, z) \mapsto (x/\bar{l}_\nu, y u_\tau(X^+)/\nu, z/\bar{l}_\nu) =: (x^+, \eta^+, z^+). \quad (2.6)$$

Note that in the definition of  $\eta^+$ , the argument in the friction velocity  $u_\tau$  is  $X^+ = \epsilon x/\bar{l}_\nu = x/L$ .

The plan now is to first transform the incompressible Navier-Stokes equations from Cartesian to  $(x^+, \eta^+, z^+)$  coordinates and then insert the scaling hypothesis (2.5) into the result.

To transform the mass and momentum equations to the new coordinates (2.6), first

note that derivatives transform as

$$\begin{aligned}\frac{\partial}{\partial x} &\mapsto 1/\bar{l}_\nu \frac{\partial}{\partial x^+} + \epsilon/\bar{l}_\nu \eta^+ \frac{\partial \log(u_\tau)}{\partial X^+} \frac{\partial}{\partial \eta^+} \\ \frac{\partial}{\partial y} &\mapsto 1/l_\nu(X^+) \frac{\partial}{\partial \eta^+} \\ \frac{\partial}{\partial z} &\mapsto 1/\bar{l}_\nu \frac{\partial}{\partial z^+},\end{aligned}$$

where  $l_\nu(X^+) = \nu/u_\tau(X^+)$ . Inserting the transformations in the continuity equation

$$\frac{\partial u_i}{\partial x_i} = 0$$

gives

$$\frac{\partial u}{\partial x^+} + \bar{l}_\nu/l_\nu(X^+) \frac{\partial v}{\partial \eta^+} + \frac{\partial w}{\partial z^+} + \epsilon \eta^+ \frac{\partial \log(u_\tau)}{\partial X^+} \frac{\partial u}{\partial \eta^+} = 0. \quad (2.7)$$

After additionally scaling by the viscous time scale at  $\bar{x}$

$$\bar{t}_\nu := \frac{\nu}{u_\tau^2} \Big|_{x=\bar{x}}$$

the streamwise component of the momentum equation transforms to

$$\begin{aligned}\bar{l}_\nu/\bar{t}_\nu \frac{\partial u}{\partial t^+} + u \frac{\partial u}{\partial x^+} + \bar{l}_\nu/l_\nu(X^+) v \frac{\partial u}{\partial \eta^+} + w \frac{\partial u}{\partial z^+} + \epsilon \eta^+ \frac{\partial \log(u_\tau)}{\partial X^+} u \frac{\partial u}{\partial \eta^+} \\ + \frac{\partial p}{\partial x^+} + \epsilon \eta^+ \frac{\partial \log(u_\tau)}{\partial X^+} \frac{\partial p}{\partial \eta^+} - \nu/\bar{l}_\nu \frac{\partial^2 u}{\partial x^+ \partial x^+} - \nu/\bar{l}_\nu \frac{\partial^2 u}{\partial z^+ \partial z^+} \\ - \nu \bar{l}_\nu/l_\nu^2(X^+) \frac{\partial^2 u}{\partial \eta^+ \partial \eta^+} - 2\epsilon \nu \eta^+ /l_\nu(X^+) \frac{\partial \log(u_\tau)}{\partial X^+} \frac{\partial^2 u}{\partial x^+ \partial \eta^+} = 0,\end{aligned} \quad (2.8)$$

where the  $\mathcal{O}(\epsilon^2)$  terms have been dropped. Similar terms appear for the other components. So far, the equations have simply been recast into new coordinates. In (2.8), the advective derivative is on the first line while the pressure gradient is on the second; the viscous terms are on both the second and third.

The next step is to hypothesize that the velocity and pressure fields scale with  $u_\tau(X^+)$  and  $u_\tau^2(X^+)$ , respectively, as in (2.5). Using the superscript ‘+’ to denote this scaling, the continuity equation (2.7) becomes

$$\frac{\partial u^+}{\partial x^+} + \bar{l}_\nu/l_\nu(X^+) \frac{\partial v^+}{\partial \eta^+} + \frac{\partial w^+}{\partial z^+} + \epsilon \frac{\partial \log(u_\tau)}{\partial X^+} \frac{\partial}{\partial \eta^+} (\eta^+ u^+) = 0. \quad (2.9)$$

Recall that the multiscale assumption underlying this analysis asserts that, at any given streamwise location, the  $\epsilon$ -dependent slow-growth terms evolve over asymptotically large distances relative to the local viscous length scale; in particular then at  $x = \bar{x}$ , (2.9) simplifies to

$$\left( \frac{\partial u^+}{\partial x^+} + \frac{\partial v^+}{\partial y^+} + \frac{\partial w^+}{\partial z^+} \right) + \epsilon \frac{\partial}{\partial y^+} (y^+ u^+) = 0, \quad (2.10)$$

since at  $x = \bar{x}$

$$\frac{\partial \log(u_\tau)}{\partial X^+} = \frac{\bar{l}_\nu}{\epsilon} \frac{\partial \log(u_\tau)}{\partial x} (\bar{x}) = 1$$

and  $l_\nu(X^+) = \bar{l}_\nu$ . Note that in (2.10),  $y^+$  denotes  $\eta^+$  at  $\bar{x}$ . The same procedure of



inserting the scaling assumptions and insisting they hold at  $x = \bar{x}$  results in

$$\begin{aligned} & \frac{\partial u_i^+}{\partial t^+} + u^+ \frac{\partial u_i^+}{\partial x^+} + v^+ \frac{\partial u_i^+}{\partial y^+} + w^+ \frac{\partial u_i^+}{\partial z^+} + \epsilon u^+ \frac{\partial}{\partial y^+} (y^+ u_i^+) \\ & + \left( \frac{\partial p^+}{\partial x^+} + \epsilon \left( y^+ \frac{\partial p^+}{\partial y^+} + 2p^+ \right) \right) \delta_{1i} + \frac{\partial p^+}{\partial y^+} \delta_{2i} + \frac{\partial p^+}{\partial z^+} \delta_{3i} \\ & - \left( \frac{\partial^2}{(\partial x^+)^2} + \frac{\partial^2}{(\partial y^+)^2} + \frac{\partial^2}{(\partial z^+)^2} \right) u_i^+ - 2\epsilon \frac{\partial^2}{\partial x^+ \partial y^+} (y^+ u_i^+) = 0 \end{aligned} \quad (2.11)$$

for the  $i$ -th component of the momentum equation; again the  $\mathcal{O}(\epsilon^2)$  have been neglected.

Equation (2.11) contains  $\mathcal{O}(\epsilon)$  terms originating from convective, pressure, and viscous effects. Recall, however, that the contribution to the mean stress balance from the viscous streamwise growth term (the final term in the integral in (2.4)) is negligible in the adverse-pressure gradient flows discussed in Section 2.2. Hence, the  $\mathcal{O}(\epsilon)$  viscous terms are dropped, as was done in Spalart (1988). Similarly, the  $\mathcal{O}(\epsilon)$  pressure terms are dropped, since the pressure gradient is assumed to be constant over the length scales of the near-wall patch domain. Thus, only the convective growth terms remain.

Using index notation, the simplified momentum equation becomes

$$\frac{\partial u_i^+}{\partial t^+} + u_j^+ \frac{\partial u_i^+}{\partial x_j^+} + \frac{\partial p^+}{\partial x_i^+} - \frac{\partial^2 u_i^+}{\partial x_j^+ \partial x_j^+} + \epsilon u^+ \frac{\partial}{\partial y^+} (y^+ u_i^+) = 0. \quad (2.12)$$

For numerical purposes, it is useful to rewrite (2.12) in conservative form. Because of the slow-growth contribution to the continuity equation (2.10), however, an additional  $\mathcal{O}(\epsilon)$  convective term appears:

$$\frac{\partial u_i^+}{\partial t^+} + \frac{\partial}{\partial x_j^+} (u_i^+ u_j^+) + \frac{\partial p^+}{\partial x_i^+} - \frac{\partial^2 u_i^+}{\partial x_j^+ \partial x_j^+} + \epsilon \left( u^+ u_i^+ + \frac{\partial}{\partial y^+} (y^+ u^+ u_i^+) \right) = 0. \quad (2.13)$$

Note that this multiscale analysis was carried out starting with the incompressible Navier-Stokes equations in Cartesian coordinates written in convective form. If instead one starts with the equations written in conservative form, makes the same coordinate transformation (2.6) and scaling assuming (2.5), and retains only the  $\mathcal{O}(\epsilon)$  convective terms, then equation (2.13) will result.

#### 2.4. *A priori test of SG model*

From the scaling assumption (2.5) the velocity components  $u_i^+$  are homogeneous in the stream and spanwise directions. At statistical equilibrium, the slow-growth continuity equation (2.10) then implies that

$$V^+ = -\epsilon y^+ U^+. \quad (2.14)$$

Using data from the adverse-pressure-gradient simulations KS- $\beta 1$  and BVOS- $\beta 1.7$ , one can use (2.14) as an *a priori* test of the slow-growth asymptotics just detailed. Figure 3(a) illustrates how well the expression on the right-hand side of (2.14) compares to the true wall-normal mean velocity  $V^+$  in each case. The approximation is quite accurate for  $y^+ \in [0, 300]$ , although significant discrepancies appear for  $y^+ > 300$ .

Slow-growth approximations have also been evaluated a priori for the mean convection terms which were shown in Figure 2 to be important to the stress balance (2.4) of adverse-pressure-gradient turbulent boundary layers in the near-wall region. Equation

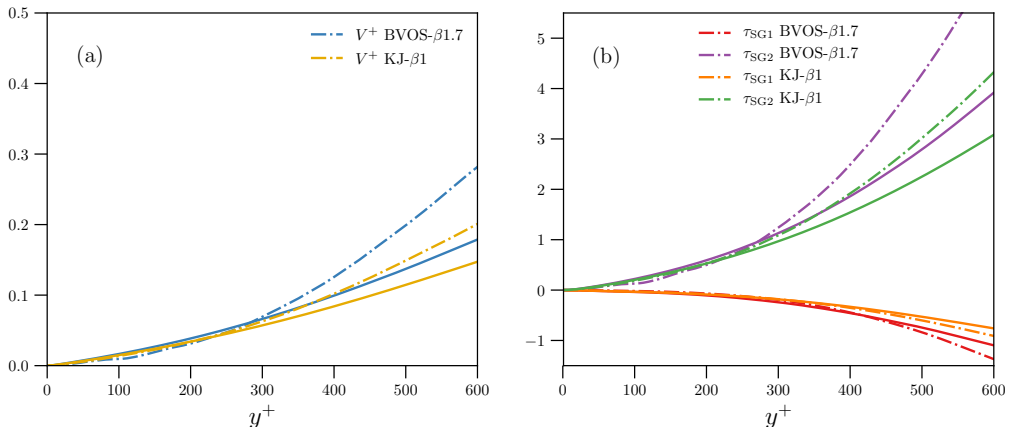


Figure 3: A priori slow-growth approximation of (a) the mean wall-normal velocity  $V^+$  and (b) the stress terms (2.15) and (2.16) for KS- $\beta 1$  and BVOS- $\beta 1.7$ . The approximations are shown in solid lines, while the quantities taken directly from the large-scale simulations are shown in dash-dotted lines.

(2.14) implies that, in viscous units,  $-\int_0^y V \partial_y U ds$  is approximated by

$$\tau_{SG1}^+ := \int_0^{y^+} \epsilon s^+ U^+ \frac{\partial U^+}{\partial s^+} ds^+, \quad (2.15)$$

while the coordinate change (2.6) and scaling assumption (2.5) imply that in viscous units,  $\int_0^y U \partial_x U ds$  is approximated by

$$\tau_{SG2}^+ := \int_0^{y^+} \epsilon U^+ \frac{\partial}{\partial s^+} (s^+ U^+) ds^+. \quad (2.16)$$

Figure 3(b) shows that (2.15) and (2.16) are indeed accurate a priori approximations of the mean convection terms in the stress balance for the near-wall region  $y^+ \leq 300$ .

### 3. Model Formulation

#### 3.1. Mathematical formulation

The goal of the computational model is to simulate the small-scale turbulent dynamics in the near-wall region as a function of an imposed gradient only in a small, rectangular domain  $\Omega = [0, L_x] \times [0, L_y] \times [0, L_z]$  localized to the boundary. Besides the physical wall at  $y = 0$  where the no-slip condition is applied, the other computational boundaries are non-physical and located where, in a large-scale simulation, there is a region of chaotic nonlinear dynamics. At the sidewalls, periodic boundary conditions are used. This is consistent with the main scaling assumption (2.5) underlying the multiscale analysis in section 2.3, since the velocity fields evolved in time are assumed to be statistically homogeneous in the stream and spanwise directions. Any statistical inhomogeneities are modeled by  $\mathcal{O}(\epsilon)$  slow-growth terms. At the upper computational boundary  $y = L_y$ , homogeneous Neumann and Dirichlet conditions are prescribed for the stream/spanwise and wall-normal velocities, respectively. Since these conditions do not allow for any momentum flux through the computational boundary, the model includes a ‘fringe region’  $y \in [L_y/2, L_y]$  in which the flow is forced to provide the momentum that is transported

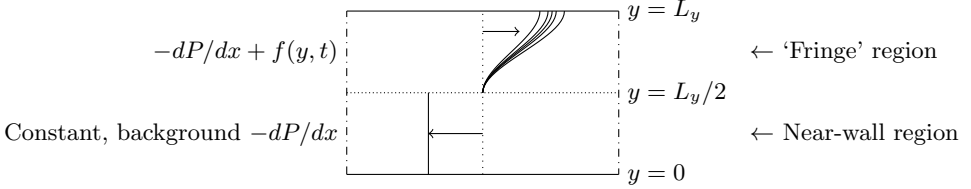


Figure 4: The fluid is subject to periodic boundary conditions at the (dash-dotted) side walls, homogeneous Dirichlet/Neumann conditions at the upper boundary  $y = L_y$ , and the no-slip condition at the wall  $y = 0$ . In addition to the constant pressure gradient assumed to be present in the near-wall layer, the model includes a time-dependent, auxiliary forcing function  $f$  (depicted here at multiple realizations in time) in a “fringe region”  $L_y/2 \leq y \leq L_y$  to make up for the momentum not transported at the computational boundary  $y = L_y$ .

into the near-wall region (see figure 4 for an illustration). The forcing  $f$  is non-zero only in the fringe region, and, given a constant pressure gradient  $dP/dx$ , it injects momentum in such a way that ensures that the model’s wall shear stress at statistical equilibrium is unity, as in Carney *et al.* (2020). Because of the  $\mathcal{O}(\epsilon)$  slow-growth contributions to the momentum equation derived in section 2.3,  $f$  is time-dependent; the precise details are given after introducing the model equations of motion below.

The model equations of motion posed on the domain  $\Omega$  are based on the slow-growth continuity (2.10) and momentum equations and (2.13) from the asymptotic analysis of Section 2.3, and they are discretized in the statistically homogeneous stream and spanwise directions with a Fourier-Galerkin method; however, there are a few differences in the equations that govern the horizontal averages

$$\bar{u}_i(y, t) = \frac{1}{L_x} \frac{1}{L_z} \int_0^{L_z} \int_0^{L_x} u_i(x, y, z, t) dx dz$$

and the fluctuations  $u'_i = u_i - \bar{u}_i$ .

Firstly, the  $(k_x, k_z) = (0, 0)$  Fourier mode of the streamwise velocity ( $\bar{u}$ ) evolves according to

$$\frac{\partial \bar{u}}{\partial t} + \frac{\partial}{\partial y} \bar{u} \bar{v} + \epsilon_L \left( \bar{u} \bar{u} + \frac{\partial}{\partial y} (y \bar{u} \bar{u}) \right) - \nu \frac{\partial^2 \bar{u}}{\partial y^2} = f - \frac{dP}{dx}, \quad (3.1)$$

which is simply the horizontal average of (2.13) (for  $i = 1$ ) with additional forcing terms.  $f$  is the fringe-region forcing whose explicit form is detailed below, while  $dP/dx$  is the constant pressure gradient driving the flow in the near-wall region. Equation (3.1) is augmented with the no-slip condition at  $y = 0$  and the homogeneous Neumann condition  $\partial_y \bar{u} = 0$  at  $y = L_y$ . Note the parameter  $\epsilon_L$  here necessarily has units of 1/length, which is emphasized with the subscript ‘ $L$ ’. After detailing the forcing  $f$ ,  $\epsilon_L$  will be related back to the nondimensional parameter (2.3).

Taking the horizontal average of the slow-growth continuity equation (2.10) gives

$$\frac{\partial \bar{v}}{\partial y} + \epsilon_L \frac{\partial}{\partial y} (y \bar{u}) = 0, \quad (3.2)$$

and the no-slip condition implies that  $\bar{v} = -\epsilon_L y \bar{u}$ , which is of course the analogue of the relation (2.14).

In contrast to  $\bar{u}$ , the evolution equation for the mean spanwise velocity  $\bar{w}$  is not given by the horizontal average of (2.13) for  $i = 3$ . Instead, the  $\mathcal{O}(\epsilon)$  contributions involving

$\overline{w}$  are neglected, as in Spalart (1988). Using

$$\overline{u'w'} = \overline{uw} - \overline{u} \overline{w},$$

$\overline{w}$  evolves as

$$\frac{\partial \overline{w}}{\partial t} + \frac{\partial}{\partial y} \overline{vw} + \epsilon_L \left( \overline{u'w'} + \frac{\partial}{\partial y} (y \overline{u'w'}) \right) - \nu \frac{\partial^2 \overline{w}}{\partial y^2} = 0,$$

with the no-slip condition and a homogeneous Neumann condition at  $y = 0$  and  $y = L_y$ , respectively. This can be justified by the fact that the mean spanwise velocity  $W = 0$  in each of the large scale simulations listed in table 1; it does not grow. Moreover, numerical stability issues can arise if one includes the  $\mathcal{O}(\epsilon)$  contributions involving  $\overline{w}$ , since the laminar equation for  $\overline{w}$

$$\frac{\partial \overline{w}}{\partial t} - \nu \frac{\partial^2 \overline{w}}{\partial y^2} = -\epsilon_L \overline{u} \overline{w}$$

can exhibit exponential growth. Indeed, if  $\epsilon_L < 0$  (as is the case for each large-scale simulation in table 1) and  $\overline{u}$  is frozen in time, then  $\overline{w} \sim \exp(-\epsilon_L \overline{u} t)$ .

The Fourier modes  $(k_x, k_z) \neq (0, 0)$  evolve as

$$\frac{\partial u_i}{\partial t} + \frac{\partial}{\partial x_j} (u_i u_j) + \epsilon_L \left( u u_i + \frac{\partial}{\partial y} (y u u_i) \right) + \frac{\partial p}{\partial x_i} - \nu \frac{\partial^2 u_i}{\partial x_j \partial x_j} = 0 \quad (3.3)$$

$$\frac{\partial u_i}{\partial x_i} = 0, \quad (3.4)$$

in which the  $\mathcal{O}(\epsilon)$  contribution to continuity is neglected, as in Spalart (1988). This appears to be a sensible approximation for boundary layers with mild  $\beta$  values; recall from figure 2 that the streamwise evolution of the turbulent kinetic energy made a negligible contribution to the mean stress balances of the KS- $\beta 1$  and BVOS- $\beta 1.7$  flows in the near-wall region. The slow-growth momentum equation (3.3) is augmented with the no-slip condition  $u_i = 0$  at  $y = 0$  and the no-flux conditions

$$v = \frac{\partial u}{\partial y} = \frac{\partial w}{\partial y} = 0 \quad \text{at } y = L_y.$$

The model equations are solved numerically using the velocity-vorticity formulation of Kim *et al.* (1987), which is derived from (3.3) and (3.4) in the usual way (Lee 2015).

With all the equations of motion determined, the details of the forcing function  $f$  in the mean streamwise evolution equation (3.1) can now be specified. Its role is to provide momentum that will be transported to the near-wall region, and it is non-zero only in the fringe region  $y > L_y/2$ . It is constructed in such a way that, for a given set of values  $dP/dx$  and  $\epsilon_L$ , the model's equilibrium wall shear stress equals unity.

More specifically, from (3.1), the model's mean streamwise stress balance is

$$\tau_w + \frac{dP}{dx} y = \tau_{\text{model}}(y) + \int_0^y f \, ds, \quad (3.5)$$

where, from the relation  $V = -\epsilon_L y U$  (which follows from (3.2)), the model stress  $\tau_{\text{model}}$  is

$$\tau_{\text{model}}(y) = \nu \frac{\partial U}{\partial y} - \langle u'v' \rangle - \epsilon_L \left( \int_0^y [U^2 + \langle u'u' \rangle] \, ds + y \langle u'u' \rangle \right). \quad (3.6)$$

The no-flux boundary conditions imply that at  $y = L_y$ , (3.5) becomes

$$\int_0^{L_y} f \, dy = \tau_w + \frac{dP}{dx} L_y + \epsilon_L \left( \int_0^{L_y} [U^2 + \langle u'u' \rangle] \, dy + L_y \langle u'u' \rangle \Big|_{y=L_y} \right).$$

---

Model case	$dP^+/dx^+$	$\epsilon$
NWP-ZPG	0	0
NWP- $\beta 1$	$5.503 \cdot 10^{-3}$	0
NWP- $\beta 1.7$	$8.981 \cdot 10^{-3}$	0
SG-NWP-ZPG	0	$-2.985 \cdot 10^{-7}$
SG-NWP- $\beta 1$	$5.503 \cdot 10^{-3}$	$-9.430 \cdot 10^{-6}$
SG-NWP- $\beta 1.7$	$8.981 \cdot 10^{-3}$	$-1.064 \cdot 10^{-5}$

---

Table 2: Imposed pressure gradient and slow-growth parameters for the model cases presented. Each value was chosen to match the corresponding one from the large-scale simulations listed in table 1.

If one then constrains  $f$  to satisfy

$$\int_0^{L_y} f dy = 1 + \frac{dP}{dx} L_y + \epsilon_L \left( \int_0^{L_y} [U^2 + \langle u' u' \rangle] ds + L_y \langle u' u' \rangle \Big|_{y=L_y} \right), \quad (3.7)$$

the desired result  $\tau_w = 1$  will follow. Assuming ergodicity, the identity

$$\langle A \rangle = \langle \overline{A} \rangle$$

is true for any field  $A$ . Hence, if at each point in time

$$\int_0^{L_y} f(y, t) dy = 1 + \frac{dP}{dx} L_y + \epsilon_L \left( \int_0^{L_y} \overline{uu}(y, t) dy + L_y \overline{u'u'}(L_y, t) \right) \quad (3.8)$$

holds, then (3.7) will result at equilibrium. The functional form of  $f$  is described in section 3.3 below. If one additionally sets the kinematic viscosity  $\nu = 1$ , then at equilibrium the model is scaled in viscous units, and the parameter  $\epsilon_L$  reduces to the nondimensional  $\epsilon$  introduced in equation (2.3).

### 3.2. Physical parameters

Each slow-growth near-wall patch model case is parameterized by two inputs; they are the constant mean pressure gradient scaled in wall units  $dP^+/dx^+$  and the asymptotic growth parameter  $\epsilon$  given by (2.3). The values for the various model cases presented—two adverse-pressure-gradient cases and one zero-pressure-gradient case—are shown in table 2. Note that for each pressure gradient value there is a model case both with ( $\epsilon \neq 0$ ) and without ( $\epsilon = 0$ ) growth effects included. Figure 5 illustrates the statistically converged stress balances for the three slow-growth model cases. As the imposed pressure gradient  $dP^+/dx^+$  increases, the total momentum transport in the near-wall region increases, as noted in section 2.2.

### 3.3. Computational parameters and numerical implementation

The remaining model parameters, consistent for all simulation cases, are summarized in table 3 and are identical to those used in Carney *et al.* (2020). In particular the size of the rectangular domain  $\Omega$  is taken to be  $L_x^+ = L_z^+ = 1500$  and  $L_y^+ = 600$ , selected based on the spectral analysis of Lee & Moser (2019). Their work suggests that, at least for the mild favorable-pressure-gradient cases considered, the contributions to the turbulent kinetic energy from modes with wavelengths  $\lambda^+ < 1000$  are universal and  $Re_\tau$

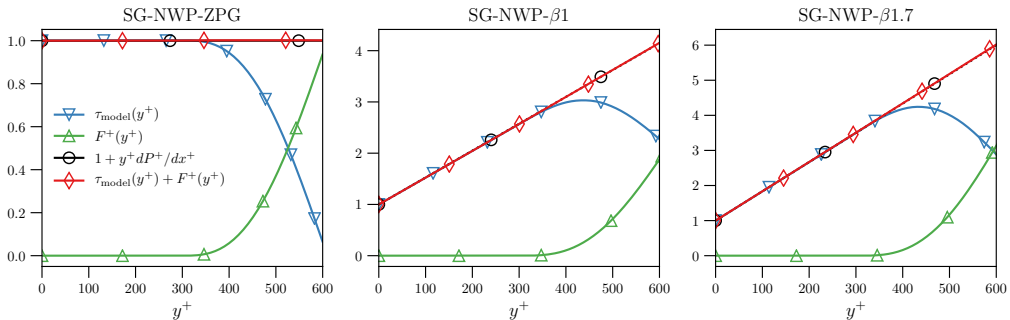


Figure 5: For each case in table 1, the model stress  $\tau_{\text{model}}^+(y^+)$  (equation (3.6)) agrees with the target stress profile  $\tau_{\text{target}}^+(y^+) = 1 + y^+ dP^+/dx^+$  for  $y^+ \in [0, 300]$ , while in the fringe region  $y^+ \in [300, 600]$ , the primitive  $F^+(y^+)$  of the forcing function  $f$  supplies momentum flux so that  $\tau_{\text{model}}^+(y^+) + F^+(y^+)$  agrees with the target stress throughout the entire domain  $y^+ \in [0, 600]$ .

---

$L_x^+ = L_z^+$	$L_y^+$	$N_x$	$N_z$	$N_y$	$\Delta x^+$	$\Delta z^+$	$\Delta y_w^+$
1500	600	120	256	192	12.5	5.86	0.002817

---

Table 3: Summary of simulation parameters consistent for all simulation cases;  $N_x$  and  $N_z$  refer to the number of Fourier modes, while  $N_y$  is the number of B-spline collocation points.  $\Delta x = L_x/N_x$  and similarly for  $\Delta z$ .  $\Delta y_w$  is the collocation point spacing at the wall.

---

independent in the region  $y^+ \lesssim 300$ . Accordingly,  $L_y^+$  is taken to be  $2 \cdot 300 = 600$  to allow for a sufficiently large fringe region to mollify the effect of the non-physical computational boundary at  $y = L_y$  (see figure 4). The values  $L_x^+ = L_z^+ = 1500$  were chosen because they were found to be the smallest domain sizes capable of reproducing the universal small-scale turbulent kinetic energies identified in the channel flow simulations of Lee & Moser (2019) (see §3.3 in Carney *et al.* (2020)). The majority of statistics reported in this work were from simulations with these stream and spanwise dimensions; however, a range of values larger than 1500 were also explored to assess the dependence of the model statistics on the choice of  $L_x$  and  $L_z$ . In general, the differences between statistics from these simulations were quite small. For completeness, the results are documented in the appendix (A).

For a given selection of model parameters ( $dP^+/dx^+$ ,  $\epsilon$ ), the forcing function  $f$  responsible for providing momentum flux to the near-wall region is constrained at each timestep to satisfy (3.8); otherwise, however, it is not uniquely specified. For the simulations reported here,  $f$  is taken to be  $f(y, t) = \psi(t)g(y)$ , where  $g$  is a piecewise cubic function

$$g(y) = \begin{cases} 4/L_y^4 (L_y - 2y)^2 (5L_y - 4y), & y \in [L_y/2, L_y] \\ 0, & y \in [0, L_y/2] \end{cases} \quad (3.9)$$

which satisfies

$$\int_{L_y/2}^{L_y} g(y) dy = 1 \quad (3.10)$$

and  $g(L_y/2) = g'(L_y/2) = g'(L_y) = 0$ , so that the transition in forcing from the near-

wall region to the fringe region is smooth. In general, other function forms for  $g$  are of course possible, and in particular a quadratic profile satisfying (3.10) and  $g(L_y/2) = g'(L_y/2) = 0$  was also implemented with no discernible changes in the statistics in the near-wall region  $y^+ \in [0, 300]$ . The time-dependent function  $\psi$  is defined as

$$\psi(t) = 1 + \frac{dP}{dx} L_y + \epsilon_L \left( \int_0^{L_y} \overline{uu}(y, t) dy + L_y \overline{u'u'}(L_y, t) \right), \quad (3.11)$$

which is simply the right hand side of the forcing constraint (3.8). Together, (3.10) and (3.11) ensure that the constraint (3.8) indeed holds.

As mentioned in §3.1 above, the model is solved numerically using the velocity-vorticity formulation due to Kim *et al.* (1987). The numerical method is identical to the one employed by Carney *et al.* (2020) and Lee & Moser (2015), that is, a Fourier-Galerkin method and a seventh-order B-spline collocation method for the stream/spanwise directions and wall-normal direction, respectively. The equations of motion are integrated in time with a low-storage, third-order Runge-Kutta (RK) method that treats diffusive terms implicitly and convective terms explicitly (Spalart *et al.* 1991). Note that the forcing term  $f(y, t)$  in the evolution equation (3.1) for  $\bar{u}$  is a nonlinear (and nonlocal) expression, and it is thus treated explicitly in the RK scheme, like the other nonlinear terms.

The computational resolution in both time and space is chosen to be consistent with that of channel flow DNS. The number of Fourier modes (and corresponding effective resolutions) used in each model simulation are listed in table 3. They are comparable with, for example, the parameters listed in table 1 in Lee & Moser (2015). Additionally, the collocation point spacing in the wall-normal direction is similar to previous DNS studies; the total number of collocation points  $N_y$  is taken to be equal to the number of collocation points below  $y^+ = 600$  in Lee & Moser (2015). They are distributed in the near-wall region according to the same (shifted and rescaled) stretching function. As in Carney *et al.* (2020), the model is implemented in a modified version of the PoongBack DNS code (Lee *et al.* 2013, 2014).

### 3.4. Statistical convergence

The method of Oliver *et al.* (2014) is used to assess the uncertainty in the statistics reported due to sampling error. For each  $(dP^+/dx^+, \epsilon)$  case listed in table 2, the statistics are collected by averaging in time until the estimated statistical uncertainty in the total model stress profile  $\tau_{\text{model}}(y)$  (see equation (3.6)) is less than a few per cent. Figure 6 shows that the sampling error  $|\tau_{\text{model}}^+(y^+) - \tau_{\text{target}}^+(y^+)|$  (where  $\tau_{\text{target}}(y) = \tau_w + y dP/dx$ ) is no larger than three per cent for each SG model case, and in particular the errors are smaller than the uncertainties; the errors are similarly small for the  $\epsilon = 0$  cases (not displayed).

## 4. Numerical results

Based on the underlying scale separation assumptions, the slow-growth near-wall patch (SG-NWP) model can be interpreted in one of two complementary ways. In the first, one considers it to be a model for the small-scale near-wall turbulence in a wall-bounded flow with (i) mean pressure gradient in wall units  $dP^+/dx^+$  and (ii) rate of change of the viscous length scale  $\epsilon$  identical to those imposed in the model. In this case, one aspires to have the statistics from the model agree with those of the real flow at some fixed streamwise location. Ideally this match is exact for quantities that are insensitive

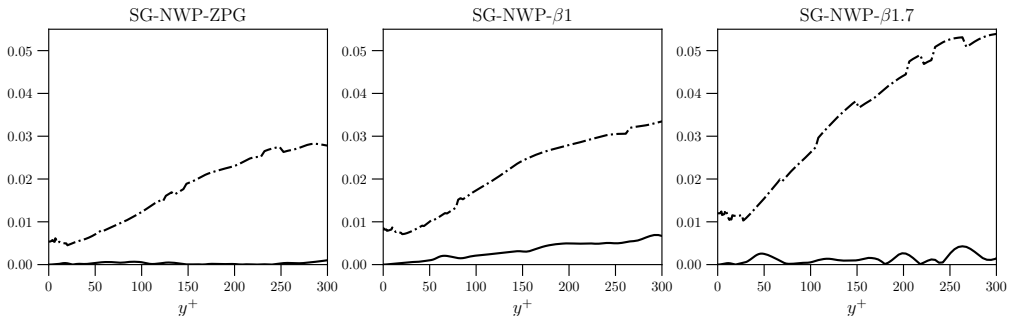


Figure 6: Statistical convergence for the slow-growth model cases listed in table 2 – solid lines: absolute error  $|\tau_{model}^+(y^+) - \tau_{target}^+(y^+)|$ , where  $\tau_{model}$  is defined in equation (3.6), and  $\tau_{target} = \tau_w + y \, dP/dx$ ; dash-dotted lines: standard deviation of the estimated statistical error for  $\tau_{model}^+$  in the region  $y^+ \in [0, 300]$ .

to the unrepresented large-scale motions, while for others the match holds after applying a high-pass filter, for example for the streamwise velocity variance, as in Lee & Moser (2019). This is the interpretation explored in the results reported here. In the second interpretation, the SG-NWP model represents the small-scale near-wall turbulence in a region of real wall-bounded turbulent flow with local (i.e. scaled with the local wall shear stress) values of  $dP^+/dx^+$  and  $\epsilon$  the same as those imposed in the model. In this case, the SG-NWP model is analogous to the universal signal of Mathis *et al.* (2011), representing the process that is modulated by large-scale outer-layer fluctuations in a real turbulent flow, and it is compatible with the quasi-steady, quasi-homogeneous description of the scale interactions in near-wall turbulence (Zhang & Chernyshenko 2016; Chernyshenko 2021). It is this second interpretation where one could potentially employ the model to inform a pressure-gradient-dependent wall-model for an LES, for example.

The statistics reported here were computed from SG-NWP model cases with three different pressure gradient values; for each value a separate simulation with  $\epsilon = 0$  was also conducted to help understand the impact of asymptotic slow-growth effects. The model statistics are compared with the three large-scale simulation cases described at the beginning of §2.2: the zero-pressure-gradient case SJM- $\beta_0$ , as well as the adverse-pressure-gradient cases KS- $\beta_1$  and BVOS- $\beta_{1.7}$ . The corresponding model cases are thus referred to as SG-NWP-ZPG, SG-NWP- $\beta_1$ , and SG-NWP- $\beta_{1.7}$  ( $\epsilon \neq 0$ ), and NWP-ZPG, NWP- $\beta_1$ , and NWP- $\beta_{1.7}$  ( $\epsilon = 0$ ). The pressure gradients imposed in the model correspond to the local values scaled in viscous units of the large-scale simulations at the streamwise location marked ‘ $\times$ ’ in figure 1, and the model’s wall-normal statistical profiles are compared to those of the large-scale simulations at these streamwise locations. All model cases are summarized in table 2.

#### 4.1. Mean velocity and shear stresses

Because the Reynolds stress of a zero-pressure-gradient boundary layer is dominated by small-scale near-wall turbulent fluctuations and growth effects are relatively insignificant, the mean velocity and Reynolds shear stress profiles from the NWP-ZPG model case are in excellent agreement with the corresponding DNS profiles (Carney *et al.* 2020). The  $\mathcal{O}(\epsilon)$  terms included in the SG-NWP-ZPG case only enhance the agreement; in particular there is a modest improvement in the Reynolds stress profile for  $y^+ \in [100, 300]$  from the NWP-ZPG case that reduces the maximum relative error from 4% to 1.3%, as shown in



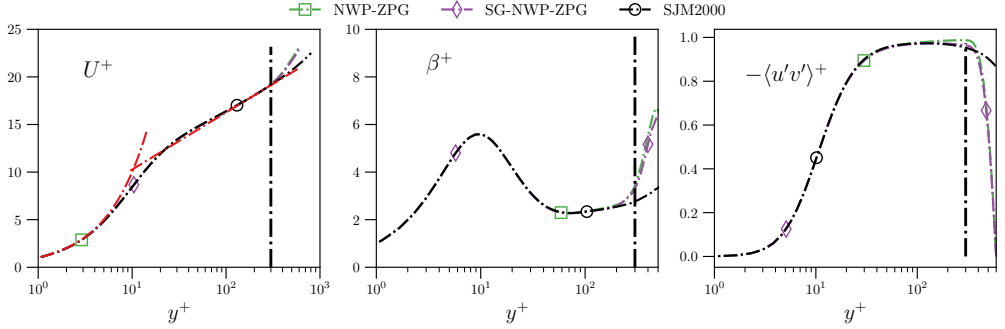


Figure 7: Mean velocity  $U^+$  (left), indicator function  $\beta^+ = y^+ \partial U^+ / \partial y^+$  (middle), and Reynolds stress  $\langle u'v' \rangle^+$  (right) versus  $y^+$  for the zero-pressure-gradient simulation cases. The vertical, black dashed-dotted lines mark the beginning of the fringe region  $y^+ = 300$ , and the law-of-the-wall  $U^+ = y^+$  and  $U^+ = (1/\kappa) \log(y^+) + B$  is also marked with a red dashed-dotted line (left), where  $\kappa = 0.384$  and  $B = 4.27$  (Lee & Moser 2015).

figure 7 (right). The slow-growth terms seem to not have an effect on the mean velocity  $U^+$ , as the NWP-ZPG and SG-NWP-ZPG profiles are nearly identical. In both cases, the relative error in  $U^+$  is less than 0.6% for  $y^+ \in [0, 300]$ , and the error is similarly small for the log-law indicator function  $\beta^+$

$$\beta^+(y^+) = y^+ \frac{\partial U^+}{\partial y^+}$$

in the range  $y^+ \in [0, 100]$ . However, in both cases there is mild disagreement of  $\beta$  in the range  $y^+ \in [100, 300]$ . As expected, the profiles diverge for  $y^+ > 300$ ; recall that  $\langle u'v' \rangle$  necessarily vanishes as a consequence of the  $v = 0$  condition posed (for Fourier modes  $(k_x, k_z) \neq (0, 0)$ ) at the upper computational boundary  $y = L_y$ .

Since growth effects fundamentally alter the balance of momentum transport in the near-wall region for adverse-pressure gradient boundary layers (recall figure 2), the model cases NWP- $\beta_1$  and NWP- $\beta_{1.7}$  that do not account for these effects are not expected to accurately reproduce the Reynolds shear stress profiles from the corresponding DNS and WRLES cases KS- $\beta_1$  and BVOS- $\beta_{1.7}$ . Figure 8 indeed shows that this is the case; when  $\epsilon = 0$ , the model severely overestimates the target profiles for  $y^+ \in [70, 300]$ . Including the  $\mathcal{O}(\epsilon)$  terms from the slow-growth analysis, however, leads to a significant improvement, as the SG-NWP- $\beta_1$  and SG-NWP- $\beta_{1.7}$  model cases both have a maximum error of about 9% and 7%, respectively, for  $y^+ \in [0, 300]$ . This remarkable improvement demonstrates that the SG-NWP model's  $\mathcal{O}(\epsilon)$  terms, as well as the forcing function  $f$  in the fringe-region  $300 \leq y^+ \leq 600$ , provide a good approximation of the momentum transport environment present in real, spatially developing wall-bounded turbulent flows with mild adverse-pressure gradients.

Similar to the zero-pressure-gradient case, the mean velocity and log-law indicator profiles for the adverse-pressure-gradient model flows are essentially identical whether or not slow-growth effects are included. For all four adverse-pressure gradient model cases, the relative error in the mean velocity profile  $U^+$  is less than 6% in the near-wall region  $y^+ \in [0, 300]$ . The error in the log-law indicator function  $\beta^+$  is similarly small for  $y^+ \in [0, 80]$ , while each model case underpredicts  $\beta$  for  $y^+ \in [80, 300]$ . However, this underprediction appears to be slightly worse for the SG-NWP cases than for those with  $\epsilon = 0$ . From the mean stress balance (3.5), for  $\epsilon = 0$ , overprediction of the Reynolds shear

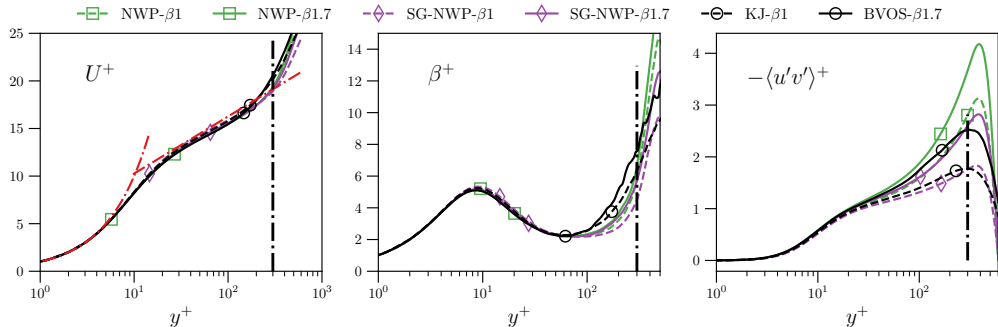


Figure 8: Mean velocity  $U^+$  (left), indicator function  $\beta^+ = y^+ \partial U^+ / \partial y^+$  (middle), and Reynolds stress  $\langle u'v' \rangle^+$  (right) versus  $y^+$  for the adverse-pressure-gradient simulation cases. The vertical, black dashed-dotted lines mark the beginning of the fringe region  $y^+ = 300$ , and the law-of-the-wall  $U^+ = y^+$  and  $U^+ = (1/\kappa) \log(y^+) + B$  is also marked with a red dashed-dotted line (left), where  $\kappa = 0.384$  and  $B = 4.27$  (Lee & Moser 2015).

stress implies underprediction of the mean viscous stress, however, the slow-growth terms present in (3.5) appear to be responsible for the underprediction when  $\epsilon \neq 0$ , given that the Reynolds stress is more accurate.

#### 4.2. Velocity variances

For a wall-bounded flow in a full size domain, the low-wavenumber contributions to the Reynolds stress represent the mean influences of the large-scale structures on the near-wall dynamics. It is well established that for channel and zero-pressure-gradient boundary layer flows, these low-wavenumber features of the near wall flow depend on  $Re_\tau$  (Hutchins & Marusic 2007; Marusic *et al.* 2010a; Lee & Moser 2017; Samie *et al.* 2018; Lee & Moser 2019). Their contribution to the turbulent kinetic energy and their modulation of the small-scale, high-wavenumber energy both increase with increasing  $Re_\tau$ . Experimental (Harun *et al.* 2013; Sanmiguel Vila *et al.* 2017, 2020) and computational (Lee 2017; Yoon *et al.* 2018; Tanarro *et al.* 2020; Pozuelo *et al.* 2022) studies have demonstrated that a similar result holds for adverse-pressure-gradient boundary layers; increasing the pressure gradient parameter  $\beta$  leads to a significant enhancement of the large-scale energy, both in the outer layer and in the near-wall region.

The slow-growth near-wall patch model, by design, cannot accurately represent these large-scale structures, as it instead seeks to isolate the dynamics of the near-wall small-scales associated with the autonomous cycle of Jiménez & Pinelli (1999) from their influence. Since the stream and spanwise velocity variances in both the zero and adverse pressure gradient boundary layers considered here are known to depend on low-wavenumber contributions, the corresponding model profiles are not expected to be accurate. Figure 9 shows this is indeed the case. Although both the NWP-ZPG and SG-NWP-ZPG  $\langle u'u' \rangle$  profiles appear to be in excellent agreement with the corresponding profile from Sillero *et al.* (2013), this is a serendipitous coincidence. For an experiment or simulation at a larger  $Re_\tau$ , the streamwise velocity variance will grow (see figure 2 in Samie *et al.* (2018), for example), but it will be modeled by a similar SG-NWP flow; although  $\epsilon$  may differ slightly, the pressure gradient will be the same. Similarly, at first glance, the model  $\langle u'u' \rangle$  profiles in the adverse-pressure-gradient cases (bottom row of figure 9) are seen to be significantly larger than their large-scale simulation counterparts. However, it should be noted that the KS- $\beta 1$  and BVOS- $\beta 1.7$  simulations are at relatively

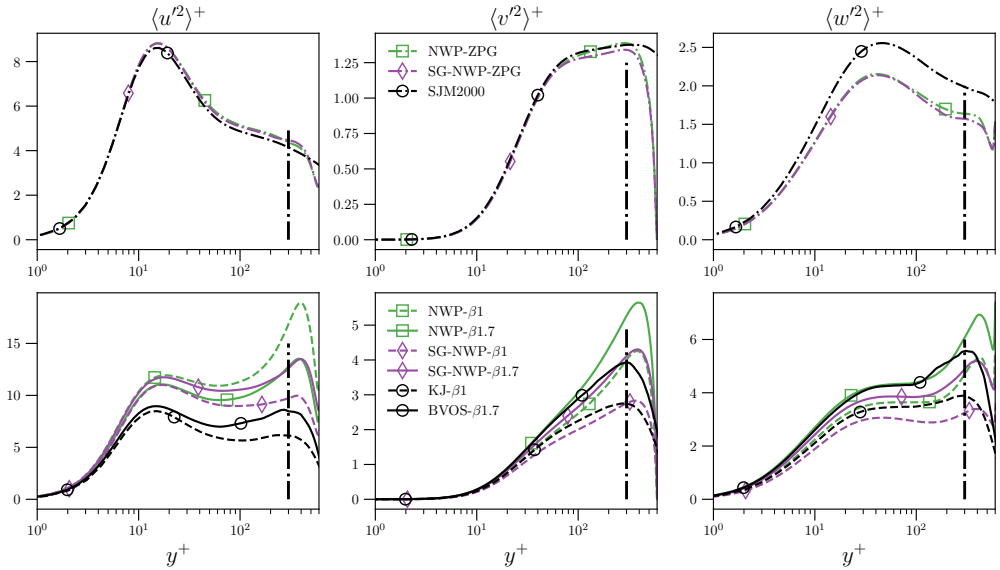


Figure 9: Velocity variances  $\langle u'_\alpha u'_\alpha \rangle$  versus  $y^+$  for zero-pressure-gradient (top row) and adverse pressure gradient (bottom row) simulations. The vertical, black dash-dotted lines mark the beginning of the fringe region  $y^+ = 300$ .

low  $Re_\tau$  (see table 1); at fixed  $\beta$  values but larger  $Re_\tau$ , the profiles would be larger (Sanmiguel Vila *et al.* 2020; Pozuelo *et al.* 2022).

In contrast to the stream and spanwise velocity variances, the impact of large-scale motions on the wall-normal velocity variance for zero and adverse pressure gradient boundary layers is less well-documented. For channel flows, Lee & Moser (2019) established that the  $\langle v'v' \rangle$  energy density in the near-wall region is concentrated primarily at wavelengths less than 1000 in viscous units, and hence the near-wall patch profiles from Carney *et al.* (2020) were indeed in agreement with those from large-scale simulations. Figure 9 suggests a similar result holds true for the near-wall region of adverse-pressure-gradient boundary layers. Although the agreement is not as good as the zero-pressure-gradient cases, the SG-NWP model  $\langle v'v' \rangle$  profiles compare reasonably well with the KS- $\beta 1$  and BVOS- $\beta 1.7$  data; the maximum relative error for  $y^+ \in [0, 300]$  is 14% and 8.5%, respectively. The NWP model without slow-growth effects, however, overpredicts the adverse-pressure-gradient wall-normal velocity variance, similar to the Reynolds shear stress profiles, illustrating the impact of the streamwise development of the mean wall shear stress  $\tau_w$  on the near-wall turbulent kinetic energy.

#### 4.3. Small-scale turbulent kinetic energy

Universal small-scale dynamics in the near-wall region associated with the autonomous cycle of Jiménez & Pinelli (1999) have been identified in channels (Lee & Moser 2019) and zero-pressure-gradient boundary layers (Samie *et al.* 2018) by applying a high-pass filter to the energy spectral density. Increases in the near-wall, small-scale energy have also been reported in adverse-pressure-gradient boundary layers due to amplitude modulation effects (Harun *et al.* 2013; Lee 2017; Yoon *et al.* 2018). Sanmiguel Vila *et al.* (2020) explicitly computed small-scale contributions to the near-wall turbulent kinetic energy. Using a cutoff wavelength of  $\lambda_x^+ \approx 4300$ , they found a collapse in the peak of the small-

scale contribution to  $\langle u'u' \rangle^+$  at  $y^+ \approx 15$  for a range of  $\beta$  values from 0 to approximately 2.2. In contrast, Lee (2017) found that the small-scale contributions to the streamwise velocity variance increased with the pressure gradient, however, this result was based on a much more restrictive high-pass filter; all contributions from spanwise wavelengths  $\lambda_z^+ \gtrsim 180$  were filtered out. Using the same filter as Carney *et al.* (2020) defined by (4.1) below, the small-scale near-wall energy from SG-NWP flows is found to increase with increasing pressure gradient, in agreement with the conclusion from Lee (2017).

In Carney *et al.* (2020), the near-wall patch model's high-pass filtered Reynolds stress was directly compared to the filtered profiles of several channel flow DNS of (Lee & Moser 2019). After filtering out contributions from wavemodes that do not satisfy

$$\min\{|k_x|, |k_z|\} > k_{\text{cut}}, \quad (4.1)$$

where  $k_{\text{cut}} = 2\pi/\lambda_{\text{cut}}$  and  $\lambda_{\text{cut}}^+ = 1000$ , the model's Reynolds stress profiles were in close agreement with the filtered DNS profiles, indicating the NWP model successfully reproduces the universal small-scale dynamics. Although the high-pass filtered Reynolds stresses of the present slow-growth NWP model cannot be directly compared to data from the literature, we report them here nonetheless to illustrate the effect of pressure gradient and growth on the small-scale energies.

Let  $\mathcal{K}$  denote the set of all wavenumbers included in a SG-NWP simulation, and let  $k = 2\pi/\lambda_{\text{cut}}$  with  $\lambda_{\text{cut}}^+ = 1000$  as just mentioned. Define  $\mathcal{K}_{SS}$  to be the subset of  $\mathcal{K}$  with the property that  $(k_x, k_z) \in \mathcal{K}_{SS}$  if (4.1) holds. If  $E_{ij}$  denotes the Fourier transform of the two point correlation tensor

$$R_{ij}(r_x, y, r_z) = \langle u'_i(x + r_x, y, z + r_z) u'_j(x, y, z) \rangle$$

in the variables  $r_x$  and  $r_z$ , then the small-scale energies shown in figure 10 are defined to be

$$\langle u'_i u'_j \rangle_{SS}(y) = \sum_{(k_x, k_z) \in \mathcal{K}_{SS}} E_{ij}(k_x, y, k_z).$$

It is clear that, for each component  $\langle u'_\alpha u'_\alpha \rangle$ , the model's near-wall, small-scale energy increases as the pressure gradient  $dP^+/dx^+$  increases, whether or not slow-growth effects are included. The agreement between simulations with and without  $\mathcal{O}(\epsilon)$  terms is particularly strong for the streamwise small-scale energy in the region  $y^+ \lesssim 50$ , suggesting that the increase in small-scale, near-wall energy in this region can be attributed solely to the adverse pressure-gradient effects, and not to growth effects.

#### 4.4. Turbulent kinetic energy budget

The mean dynamics of the turbulent kinetic energy  $k = u'_i u'_i / 2$  are governed by the turbulent kinetic energy (TKE) budget equation

$$\frac{D \langle k \rangle}{Dt} = - \overbrace{\langle u'_i u'_j \rangle \frac{\partial U_i}{\partial x_j}}^{\mathcal{P}_k} - \overbrace{\frac{\partial \langle k u'_j \rangle}{\partial x_j}}^{T_k} + \nu \overbrace{\frac{\partial^2 \langle k \rangle}{\partial x_j \partial x_j}}^{D_k} - \overbrace{\frac{\partial \langle p' u'_j \rangle}{\partial x_j}}^{Y_k} - \overbrace{\left\langle \frac{\partial u'_i}{\partial x_j} \frac{\partial u'_i}{\partial x_j} \right\rangle}^{\epsilon_k}. \quad (4.2)$$

For a wall-bounded turbulent flow that is homogeneous in the spanwise direction and slowly developing in the streamwise direction, one can derive a 'slow-growth' version of (4.2) using the same multiscale asymptotic analysis outlined in section 2.3; namely, one transforms  $x$  and  $y$  according to (2.6) and then inserts the scaling ansatz (2.5) into the resulting equation. The resulting 'slow-growth' TKE budget equation can be shown to

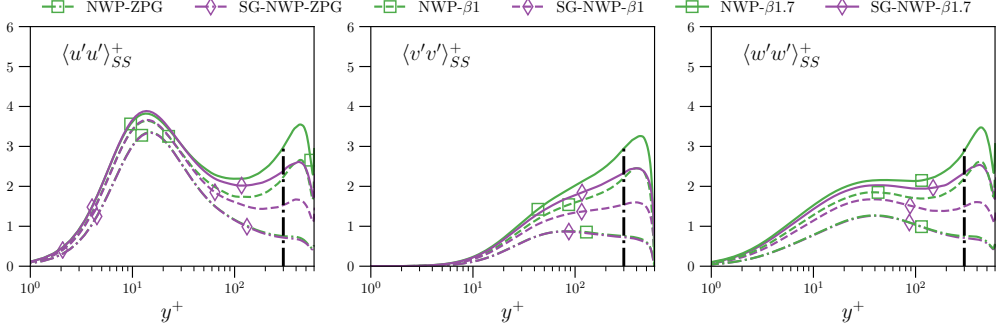


Figure 10: High-pass filtered velocity variances  $\langle u'_\alpha u'_\alpha \rangle_{SS}^+$  versus  $y^+$  for each model case listed in table 2. The vertical, black dash-dotted lines mark the beginning of the fringe region  $y^+ = 300$ .

be

$$\begin{aligned}
 \overbrace{2\epsilon \langle k \rangle^+ U^+}^{\text{SG Adv.}} &= - \overbrace{\left( \langle u'v' \rangle^+ \frac{\partial U^+}{\partial y^+} + \epsilon \frac{\partial}{\partial y^+} (y^+ U^+) [\langle u'u' \rangle^+ - \langle v'v' \rangle^+] \right)}^{\mathcal{P}_{k,\text{SG}}^+} \\
 &\quad - \overbrace{\left( \frac{\partial}{\partial y^+} \langle kv' \rangle^+ + 3\epsilon \langle ku' \rangle^+ + \epsilon y^+ \frac{\partial}{\partial y^+} \langle ku' \rangle^+ \right)}^{T_{k,\text{SG}}^+} \\
 &\quad - \overbrace{\left( \frac{\partial}{\partial y^+} \langle p'v' \rangle^+ + 3\epsilon \langle p'u' \rangle^+ + \epsilon y^+ \frac{\partial}{\partial y^+} \langle p'u' \rangle^+ \right)}^{\mathcal{R}_{k,\text{SG}}^+} \\
 &\quad + \overbrace{\frac{\partial^2}{(\partial y^+)^2} \langle k \rangle^+}^{D_{k,\text{SG}}^+} - \overbrace{\left\langle \frac{\partial u'_i}{\partial x_j} \frac{\partial u'_i}{\partial x_j} \right\rangle^+}^{\varepsilon_{k,\text{SG}}^+}, \tag{4.3}
 \end{aligned}$$

where the  $\mathcal{O}(\epsilon^2)$  contributions are neglected. If one alternatively starts with the slow-growth continuity (2.10) and momentum (2.11) equations from §2.3 and derives an equation governing the dynamics of  $\langle u'_i u'_i \rangle^+ / 2$  in the standard way, then, modulo  $\mathcal{O}(\epsilon^2)$  terms, nearly the same exact equation will result. The only difference is that, in this latter derivation, an extra  $\mathcal{O}(\epsilon)$  correction to the dissipation  $\varepsilon_k$  appears that is not present in (4.3). The term is proportional to  $y \langle u'_i \partial_x \partial_y u'_i \rangle$  and arises from the  $\mathcal{O}(\epsilon)$  viscous term in (2.11).

Because the SG-NWP model momentum equation (3.3) neglects some of the  $\mathcal{O}(\epsilon)$  terms that arise from the asymptotic analysis in section 2.3, there are some discrepancies between (4.3) and the model's TKE budget equation. In particular, there are discrepancies in the production  $\mathcal{P}_{k,\text{SG}}$ , as well as the turbulent and pressure transport terms  $T_{k,\text{SG}}$  and  $\mathcal{R}_{k,\text{SG}}$ . Although the errors introduced by these discrepancies are in each case relatively small, they are documented below when comparing the model's TKE budget to those of the large-scale simulations.

Firstly, since the mean advection  $U^+ \partial_x^+ \langle k \rangle^+ + V^+ \partial_y^+ \langle k \rangle^+$  from the large-scale simu-

lations and the slow-growth advection

$$2\epsilon \langle k \rangle^+ U^+$$

from the NWP model cases have a maximum value no larger than  $10^{-3}$ , they are not plotted here.

For the production  $\mathcal{P}_{k,\text{SG}}$ , the inconsistency between the continuity equations (2.10) and (3.4) leads to some ‘spurious’  $\mathcal{O}(\epsilon)$  production terms for the SG-NWP model given by

$$\mathcal{P}_{k,\text{spur}}^+ = \epsilon \left( U^+ \langle u'u' \rangle^+ + \frac{1}{2} y^+ U^+ \frac{\partial}{\partial y^+} \langle u'u' \rangle^+ \right). \quad (4.4)$$

The left half of figure 11 displays  $\mathcal{P}_k^+$  from (4.2) for the large-scale simulation cases and the sum of  $\mathcal{P}_{k,\text{SG}}^+$  from (4.3) and the spurious production (4.4) for the SG-NWP flows. Noted that for the zero and adverse-pressure gradient flows considered in this work, production is due almost exclusively to the product of  $\partial U / \partial y$  and the Reynolds shear stress. For example, this term accounts for approximately 97.5% of the total production for the three large-scale flows from table 1. Similarly, the  $\mathcal{O}(\epsilon)$  terms account for only 0.2%, 5.7%, and 4.7% of the SG model’s production  $\mathcal{P}_{k,\text{SG}}^+$  for  $y^+ \in [0, 300]$  for SG-NWP-ZPG, SG-NWP- $\beta 1$  and SG-NWP- $\beta 1.7$ , respectively, while the spurious production (4.4) is no larger than 0.1%, 3.7%, and 3.4% of  $\mathcal{P}_{k,\text{SG}}^+$  for these three model cases.

As expected, there is little difference between the SG-NWP-ZPG and NWP-ZPG production profiles, since the mean velocity gradient and Reynold shear stress profiles for both model flows are nearly identical. Both are in excellent agreement with the SJM- $\beta 0$  DNS case. For the adverse-pressure-gradient cases, the SG-NWP model’s production  $\mathcal{P}_{k,\text{SG}}^+ + \mathcal{P}_{k,\text{spur}}^+$  is consistently smaller than the corresponding cases when  $\epsilon = 0$ . At the near-wall production peak ( $y^+ \approx 12$ ), this results in better agreement with the BVOS- $\beta 1.7$  case for the SG-NWP model than the  $\epsilon = 0$  case, while for the KS- $\beta 1$  case the agreement is slightly worse. In both cases, the slow-growth model underpredicts the production profiles from the large-scale simulations for  $y^+ \gtrsim 60$ , consistent with the results for the mean streamwise velocity gradient.

Unlike the production of turbulent kinetic energy, the dissipation  $\varepsilon_k = \nu \langle \partial_j u'_i \partial_j u'_i \rangle$  does not possess any additional slow-growth contributions, as previously noted. The right half of figure 11 displays the dissipation profiles for the model and large-scale simulation cases. Although there is no discernible difference between the NWP model with and without slow-growth effects in the zero-pressure-gradient case, they do impact the model dissipation profiles in the adverse-pressure-gradient cases. In particular they effect a reduction in the maximum dissipation that occurs at the wall, resulting in better agreement with the large-scale simulation values.

Similar to the dissipation, the viscous transport does not possess any  $\mathcal{O}(\epsilon)$  slow-growth contributions. However, there are indeed some  $\mathcal{O}(\epsilon)$  ‘spurious’ contributions to the SG-NWP model’s turbulent transport given by

$$T_{k,\text{spur}}^+ = \epsilon \left( \langle k u' \rangle^+ + y^+ \left\langle k \frac{\partial u'}{\partial y} \right\rangle^+ \right) \quad (4.5)$$

that arise from omitting the  $\mathcal{O}(\epsilon)$  contribution to the fluctuating continuity equation (2.10). The omission of both this term and the  $\mathcal{O}(\epsilon)$  pressure term in (2.11) from the SG-NWP model equations also leads to some errors in the pressure transport. In particular, the model’s pressure transport does not include any slow-growth contributions, in

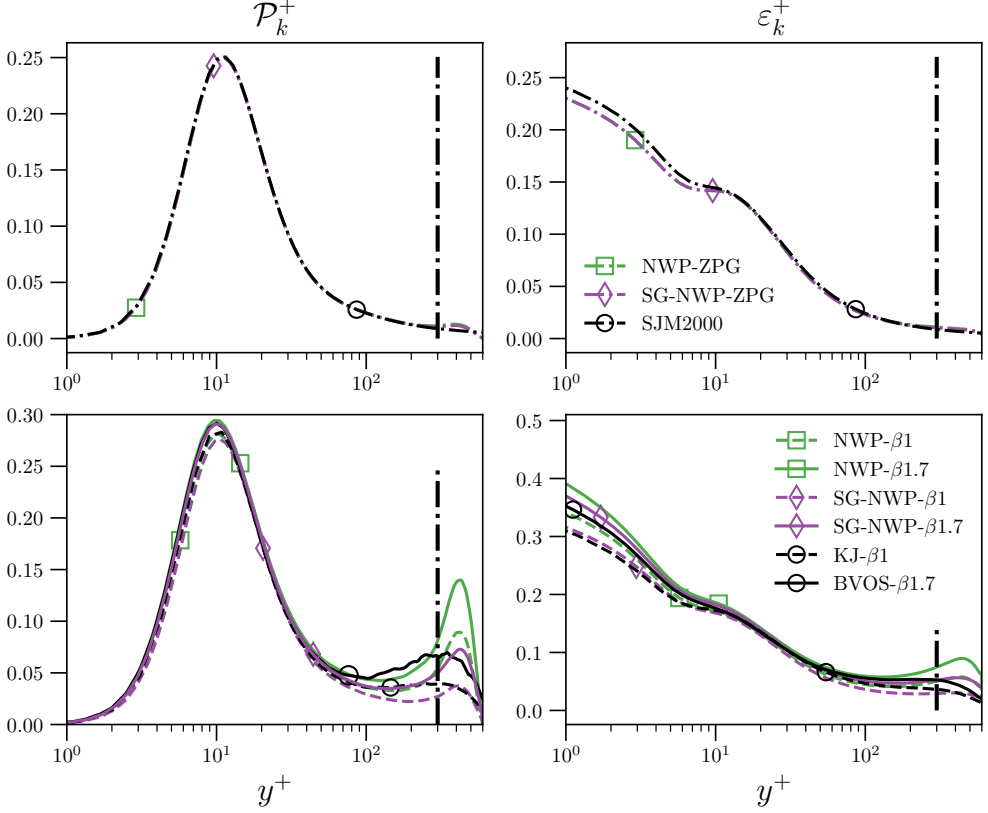


Figure 11: Left: production of TKE versus  $y^+$ , where the results from the large-scale simulations display  $\mathcal{P}_k^+$  from (4.2), while the model results display the sum of  $\mathcal{P}_{k,SG}^+$  from equation (4.3) and (4.4); right: dissipation of TKE versus  $y^+$ . For both quantities, the ZPG and APG flows are displayed in the top and bottom panels, respectively. The vertical, black dash-dotted lines mark the beginning of the fringe region  $y^+ = 300$ .

contrast to  $\mathcal{R}_{k,SG}$ , so that in effect there is a spurious contribution given by

$$\mathcal{R}_{k,spur}^+ = -\epsilon \left( 3 \langle p'u' \rangle^+ + y^+ \frac{\partial}{\partial y^+} \langle p'u' \rangle^+ \right). \quad (4.6)$$

The SG-NWP turbulent  $T_{k,SG}^+ + T_{k,spur}^+$ , pressure  $\mathcal{R}_{k,SG}^+ + \mathcal{R}_{k,spur}^+$ , and viscous  $D_{k,SG}^+$  transport profiles are displayed in figure 12 and show a reasonable agreement to the corresponding profiles  $T_k^+$ ,  $\mathcal{R}_k^+$  and  $D_k^+$  (as defined in (4.2)) from the large-scale simulations. In particular, the SG-NWP model predicts a lower value of viscous transport at the wall than the corresponding model simulations with  $\epsilon = 0$ , similar to the dissipation profiles. In contrast, the pressure transport at the wall is notably less accurate when including slow-growth effects. The error is not due to the spurious pressure transport; the spurious terms generally contribute no more than 5% to the model's total turbulent and pressure transport profiles, similar to the TKE production. Since pressure is generally responsible for enforcing continuity, it is possible that the  $\mathcal{O}(\epsilon)$  error in the fluctuating SG continuity equation (3.4) is responsible for the relatively large error, but this hypothesis was not tested.

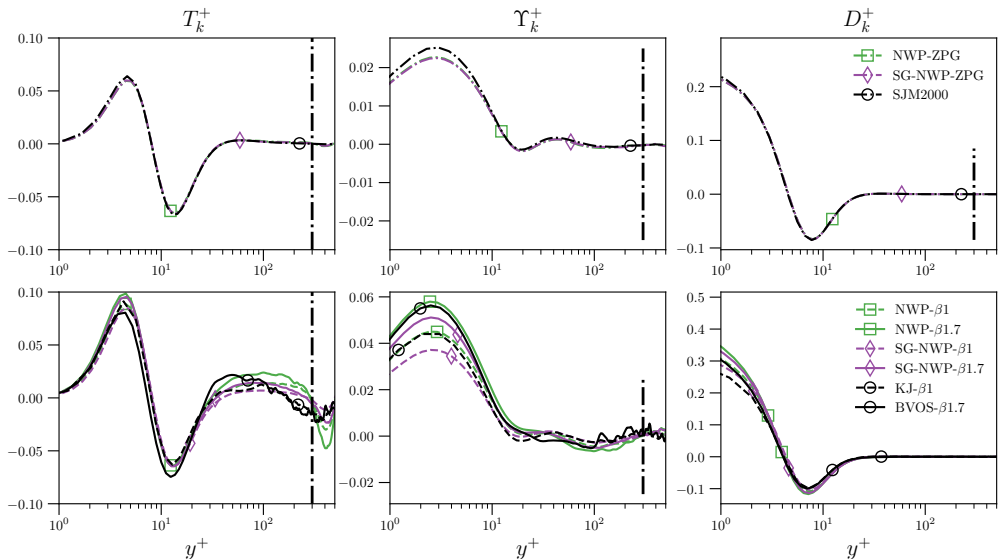


Figure 12: Turbulent (left), pressure (middle) and viscous (right) transport of TKE versus  $y^+$ . The results from the large-scale simulations display  $T_k^+$ ,  $\Upsilon_k^+$  and  $D_k^+$  from (4.2), respectively, while the model results display  $T_{k,SG}^+ + T_{k,spur}^+$ ,  $\Upsilon_{k,SG}^+ + \Upsilon_{k,spur}^+$ , and  $D_k^+$ . The verticle, black dash-dotted lines mark the beginning of the fringe region  $y^+ = 300$ .

## 5. Conclusions

The slow-growth (SG) model described here was formulated to extend the near-wall patch (NWP) representation of wall-turbulence presented in Carney *et al.* (2020) to flows with non-negligible streamwise development of mean quantities. A primary objective is to provide a computationally accessible quantitative model of wall-turbulence for such situations, for example in boundary layers with adverse-pressure-gradients. Another is to characterize the extent to which the dynamics of the small-scale motions, isolated from modulations by large-scale structures, are responsible for observed characteristics of near-wall turbulence. As in Spalart (1988) and Topalian *et al.* (2017), the model equations of motion are informed by asymptotic analysis of the Navier-Stokes (NS) equations; the fundamental assumption in the current setting is a separation between the viscous length scale and the length scale over which the mean wall shear stress evolves.

The low-order statistical profiles from the SG-NWP model compare favorably to those from large-scale simulations of zero and adverse-pressure-gradient boundary layers. In general, the agreement is particularly close for  $y^+ \lesssim 100$ . The exceptions to this result are quantities for which large scale motions make a significant contribution, for example the streamwise velocity variance. As is well-known, large-scale motions in the near-wall region increase not only with increasing Reynolds number, but also with increasing adverse-pressure-gradients. Applying a high-pass filter to the model's turbulent kinetic energy revealed that the small-scales in the near-wall region are also energized by adverse pressure gradients. Overall, the results suggest that, even at the mild  $\beta$  values considered here, the ‘universal signal’ of small-scale dynamics described by Marusic *et al.* (2010b); Mathis *et al.* (2011) (where ‘universal’ means independent of Reynolds number or external flow configuration) should also depend on both pressure gradient and the rate of change of the mean wall shear stress.

Because the SG-NWP model domain size scales in viscous units, the simulations require



orders of magnitude less computational resources compared to large-scale DNS and wall-resolved LES. For example, the model’s computational grid is approximately a factor of 5 700 and 1000 smaller than the DNS calculations of Sillero *et al.* (2013) and Kitsios *et al.* (2017), respectively, and a factor of about 144 smaller than the wall-resolved LES of Bobke *et al.* (2017). The model presented here could thus be useful in a number of different contexts.

Firstly, the model could generate data to inform a wall-modeled large-eddy simulation (WMLES) by invoking the scale-separation assumption detailed in §2.1. Based on the local values of the parameters  $\epsilon$  and  $dP^+/dx^+$  associated with the large-scale WMLES values, the model could return whatever information is needed to advance the equations of motion, for example the local wall-shear stress (Larsson *et al.* 2016) or slip-amount (Bose & Park 2018). Additionally, a statistical ensemble constructed from snapshots in time of the SG-NWP flows could potentially be useful as training data for a deep neural network approach to LES wall-modeling, as in Yang *et al.* (2019).

The SG-NWP model could additionally be deployed as a vehicle for numerical ‘experiments’ on near-wall dynamics influenced by pressure gradients, as advocated for and exemplified by Jiménez & Pinelli (1999). For example, the model could be used to study the interactions of the near-wall, small-scale dynamics with such complications as surface roughness, heat transfer, turbophoresis, or chemical reactions.

Finally, although the separation of scales on which the slow-growth model is based is well-founded for a variety of practically relevant flows, it is important to keep in mind that it is still limited to a range of pressure gradients that are not too large when scaled in viscous units. Because the viscous length scale changes more rapidly with stronger adverse pressure gradients, the asymptotic analysis on which the model is founded will no longer be valid. In particular, this makes the model inadequate to describe near-wall flow near a point of boundary layer separation.

## Acknowledgments

The work presented here was supported by the Oden Institute for Computational Engineering and Sciences. The research utilized the computing resources of the Texas Advanced Computing Center (TACC) at The University of Texas at Austin. The authors are grateful to both Callum Atkinson and Ricardo Vineusa for sharing the statistics from large-scale adverse-pressure-gradient simulations. The authors thank Gopal Yalla and Björn Engquist for insightful discussions, as well as Prakash Mohan for helpful suggestions regarding time-integration of the equations of motion.

## Declaration of interests

The authors report no conflicts of interest.

## Appendix A. Effect of wall-parallel domain size on statistical quantities

A number of simulations were conducted at fixed values of  $dP^+/dx^+$  and  $\epsilon$  that correspond to the model case SG-NWP- $\beta 1$  from table 2 to assess the dependence of the model’s statistics on the size of the near-wall patch domain size in the stream and spanwise direction. In particular, simulations were conducted with  $L_x^+ \times L_z^+ = 1500 \times 1500$  (as listed in table 3), as well as with  $1500 \times 3000$ ,  $3000 \times 3000$ , and  $4500 \times 4500$ . In each

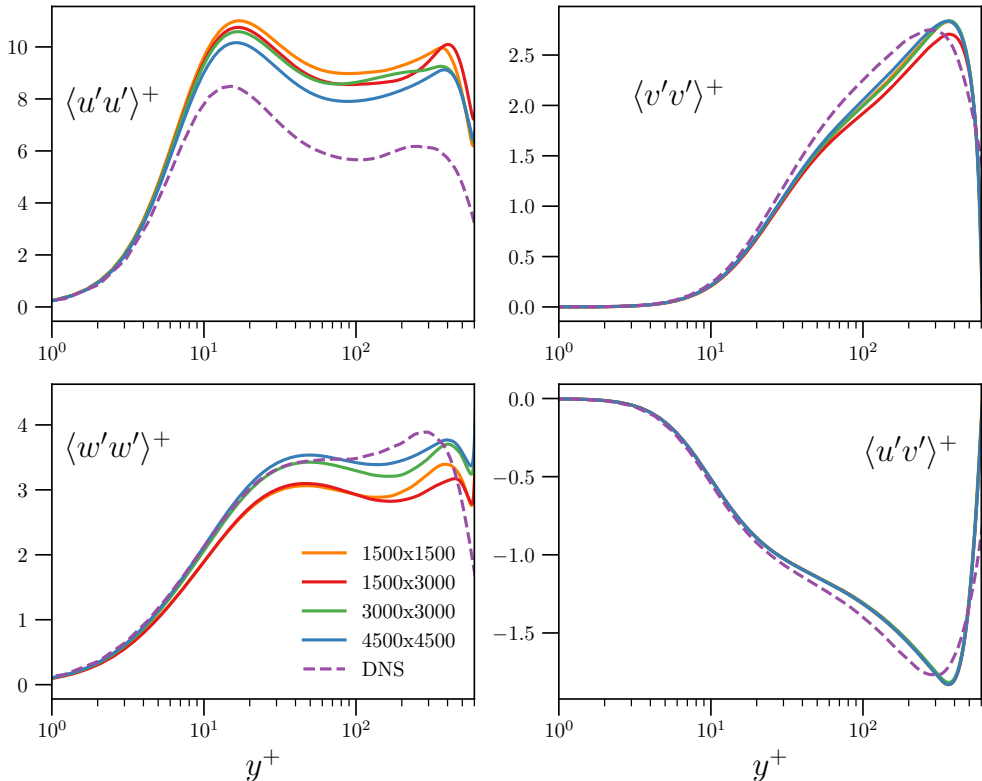


Figure 13: Reynolds stress profiles versus  $y^+$  for the DNS adverse-pressure-gradient simulation KS- $\beta$ 1 and SG-NWP- $\beta$ 1 model cases with various domain sizes  $L_x^+ \times L_z^+$ .

case, the number of Fourier modes  $N_x$  and  $N_z$  were increased proportionally to maintain the resolution  $\Delta x^+$  and  $\Delta z^+$  listed in table 3.

Figure 13 shows the Reynolds stress terms for each domain size case, as well as the DNS profiles from Kitsios *et al.* (2017). The Reynolds shear stress  $\langle u'v' \rangle$  is essentially unaffected by the domain size, while the wall-normal variances exhibit a slight increase with increasing domain size. Similarly, the streamwise velocity variances show a mild decrease with increasing domain size, while the spanwise velocity variances show a nontrivial increase and compare well with the DNS profile for  $L_x^+, L_z^+ \geq 3000$ . At these length scales, the NWP spanwise domain length is at least a third of that of the full DNS, owing to the relatively low  $Re_\tau$  at which it was conducted.

Although not shown, the effect of domain size on the mean velocity profile and its derivative is negligible, similar to the Reynolds shear stress, while the turbulent kinetic energy budget terms are also either unaffected, or show slight trends comparable to that of the wall-normal velocity variance.

## REFERENCES

- ARAYA, GUILLERMO, CASTILLO, LUCIANO, MENEVEAU, CHARLES & JANSEN, KENNETH 2011 A dynamic multi-scale approach for turbulent inflow boundary conditions in spatially developing flows. *Journal of Fluid Mechanics* **670**, 581–605.
- BOBKE, A., VINUESA, R., ÖRLÜ, R. & SCHLATTER, P. 2017 History effects and near equilibrium

- in adverse-pressure-gradient turbulent boundary layers. *Journal of Fluid Mechanics* **820**, 667–692.
- BOSE, S. T. & PARK, G. I. 2018 Wall-modeled large-eddy simulation for complex turbulent flows. *Annual Review of Fluid Mechanics* **50** (1), 535–561.
- BRADSHAW, PETER 1967 The turbulence structure of equilibrium boundary layers. *Journal of Fluid Mechanics* **29** (4), 625–645.
- CARNEY, SEAN P., ENGQUIST, BJÖRN & MOSER, ROBERT D. 2020 Near-wall patch representation of wall-bounded turbulence. *Journal of Fluid Mechanics* **903**, A23.
- CHERNYSHENKO, SERGEI 2021 Extension of QSQH theory of scale interaction in near-wall turbulence to all velocity components. *Journal of Fluid Mechanics* **916**.
- CLAUSER, FRANCIS H 1954 Turbulent boundary layers in adverse pressure gradients. *Journal of the Aeronautical Sciences* **21** (2), 91–108.
- COLONIUS, T. 2004 Modeling artificial boundary conditions for compressible flow. *Annual Review of Fluid Mechanics* **36**, 315–345.
- DEGRAAFF, D. B. & EATON, J. K. 2000 Reynolds-number scaling of the flat-plate turbulent boundary layer. *Journal of Fluid Mechanics* **422**, 319–346.
- GANAPATHISUBRAMANI, B., HUTCHINS, N., MONTY, J. P., CHUNG, D. & MARUSIC, I. 2012 Amplitude and frequency modulation in wall turbulence. *Journal of Fluid Mechanics* **712**, 61–91.
- GUARINI, STEPHEN E, MOSER, ROBERT D, SHARIFF, KARIM & WRAY, ALAN 2000 Direct numerical simulation of a supersonic turbulent boundary layer at mach 2.5. *Journal of Fluid Mechanics* **414**, 1–33.
- GUNGOR, AG, MACIEL, Y, SIMENS, MP & SORIA, J 2016 Scaling and statistics of large-defect adverse pressure gradient turbulent boundary layers. *International Journal of Heat and Fluid Flow* **59**, 109–124.
- HAMILTON, J. M., KIM, J. & WALEFFE, F. 1995 Regeneration mechanisms of near-wall turbulence structures. *Journal of Fluid Mechanics* **287**, 317–348.
- HARUN, ZAMBRI, MONTY, JASON P, MATHIS, ROMAIN & MARUSIC, IVAN 2013 Pressure gradient effects on the large-scale structure of turbulent boundary layers. *Journal of Fluid Mechanics* **715**, 477–498.
- HICKEL, S & ADAMS, NA 2008 Implicit LES applied to zero-pressure-gradient and adverse-pressure-gradient boundary-layer turbulence. *International Journal of Heat and Fluid Flow* **29** (3), 626–639.
- HOSSEINI, SEYED MOHAMMAD, VINUESA, RICARDO, SCHLATTER, PHILIPP, HANIFI, ARDESHIR & HENNINGSON, DAN S 2016 Direct numerical simulation of the flow around a wing section at moderate Reynolds number. *International Journal of Heat and Fluid Flow* **61**, 117–128.
- HUTCHINS, N. & MARUSIC, I. 2007 Large-scale influences in near-wall turbulence. *Philosophical Transactions of the Royal Society A: Mathematical, Physical and Engineering Sciences* **365**, 647–664.
- INOUE, M, PULLIN, DI, HARUN, ZAMBRI & MARUSIC, I 2013 LES of the adverse-pressure gradient turbulent boundary layer. *International journal of heat and fluid flow* **44**, 293–300.
- JEONG, J., HUSSAIN, F., SCHOPPA, W. & KIM, J. 1997 Coherent structures near the wall in a turbulent channel flow. *Journal of Fluid Mechanics* **332**, 185–214.
- JIMÉNEZ, J. & MOIN, P. 1991 The minimal flow unit in near-wall turbulence. *Journal of Fluid Mechanics* **225**, 213–240.
- JIMÉNEZ, J. & PINELLI, A. 1999 The autonomous cycle of near-wall turbulence. *Journal of Fluid Mechanics* **389**, 335–359.
- KIM, J., MOIN, P. & MOSER, R. 1987 Turbulence statistics in fully developed channel flow at low Reynolds number. *Journal of Fluid Mechanics* **177**, 133–166.
- KITSIOS, V., SEKIMOTO, A., ATKINSON, C., SILLERO, J. A., BORRELL, G., GUNGOR, A. G., JIMÉNEZ, J. & SORIA, J. 2017 Direct numerical simulation of a self-similar adverse pressure gradient turbulent boundary layer at the verge of separation. *Journal of Fluid Mechanics* **829**, 392–419.
- KNOPP, TOBIAS, BUCHMANN, NA, SCHANZ, DANIEL, EISFELD, BERNHARD, CIERPKA, CHRISTIAN, HAIN, RAINER, SCHRÖDER, ANDREAS & KÄHLER, CHR J 2015 Investigation

- of scaling laws in a turbulent boundary layer flow with adverse pressure gradient using piv. *Journal of Turbulence* **16** (3), 250–272.
- KNOPP, TOBIAS, NOVARA, M., SCHULEIN, E., SCHANZ, DANIEL, SCHRODER, ANDREAS, REUTHER, NICO & KAHLER, CHRISTIAN J 2017 Investigation of a turbulent boundary layer flow at high reynolds number using particle-imaging and implications for rans modeling. In *Tenth International Symposium on Turbulence and Shear Flow Phenomena*. Begel House Inc.
- LARSSON, JOHAN, KAWAI, SOSHI, BODART, JULIEN & BERMEJO-MORENO, IVAN 2016 Large eddy simulation with modeled wall-stress: recent progress and future directions. *Mechanical Engineering Reviews* **3** (1), 15–00418–15–00418.
- LEE, JAE HWA 2017 Large-scale motions in turbulent boundary layers subjected to adverse pressure gradients. *Journal of Fluid Mechanics* **810**, 323–361.
- LEE, JOUNG-HO & SUNG, HYUNG JIN 2009 Structures in turbulent boundary layers subjected to adverse pressure gradients. *Journal of fluid mechanics* **639**, 101–131.
- LEE, MYOUNGKYU 2015 Direct numerical simulation (DNS) for incompressible turbulent channel flow at  $Re_\tau = 5200$ . PhD thesis, The University of Texas at Austin.
- LEE, M., MALAYA, N. & MOSER, R. D. 2013 Petascale direct numerical simulation of turbulent channel flow on up to 786K cores. In *the International Conference for High Performance Computing, Networking, Storage and Analysis*, pp. 1–11. New York, New York, USA: ACM Press.
- LEE, M. & MOSER, R. D. 2015 Direct numerical simulation of turbulent channel flow up to  $Re_\tau = 5200$ . *Journal of Fluid Mechanics* **774**, 395–415.
- LEE, M. & MOSER, R. D. 2017 Large-scale Motions in Turbulent Poiseuille & Couette flows. In *Tenth International Symposium on Turbulence and Shear Flow Phenomena*. Chicago, Illinois, USA.
- LEE, M. & MOSER, R. D. 2019 Spectral analysis of the budget equation in turbulent channel flows at high reynolds number. *Journal of Fluid Mechanics* **860**, 886–938.
- LEE, M., ULERICH, R., MALAYA, N. & MOSER, R. D. 2014 Experiences from Leadership Computing in Simulations of Turbulent Fluid Flows. *Computing in Science Engineering* **16** (5), 24–31.
- LUND, THOMAS S., WU, XIAOHUA & SQUIRES, KYLE D. 1998 Generation of turbulent inflow data for spatially-developing boundary layer simulations. *Journal of Computational Physics* **140** (2), 233–258.
- MAEDER, THIERRY, ADAMS, NIKOLAUS A & KLEISER, LEONHARD 2001 Direct simulation of turbulent supersonic boundary layers by an extended temporal approach. *Journal of Fluid Mechanics* **429**, 187–216.
- MARQUILLIE, MATTHIEU, LAVAL, J-P & DOLGANOV, ROSTISLAV 2008 Direct numerical simulation of a separated channel flow with a smooth profile. *Journal of Turbulence* (9), N1.
- MARUSIC, I., MATHIS, R. & HUTCHINS, N. 2010a High Reynolds number effects in wall turbulence. *International Journal of Heat and Fluid Flow* **31** (3), 418–428.
- MARUSIC, I., MATHIS, R. & HUTCHINS, N. 2010b Predictive model for wall-bounded turbulent flow. *Science* **329** (5988), 193–196.
- MATHIS, R., HUTCHINS, N. & MARUSIC, I. 2011 A predictive inner–outer model for streamwise turbulence statistics in wall-bounded flows. *Journal of Fluid Mechanics* **681**, 537–566.
- MIZUNO, Y. & JIMÉNEZ, J. 2013 Wall turbulence without walls. *Journal of Fluid Mechanics* **723**, 429–455.
- NA, Y & MOIN, PARVIZ 1998 Direct numerical simulation of a separated turbulent boundary layer. *Journal of Fluid Mechanics* **374**, 379–405.
- OLIVER, T. A., MALAYA, N., ULERICH, R. & MOSER, R. D. 2014 Estimating uncertainties in statistics computed from direct numerical simulation. *Physics of Fluids* **26**, 035101.
- PIOMELLI, U. & BALARAS, E. 2002 Wall-layer models for large-eddy simulations. *Annual Review of Fluid Mechanics* **34** (1), 349–374.
- POZUELO, RAMÓN, LI, QIANG, SCHLATTER, PHILIPP & VINUESA, RICARDO 2022 An adverse-pressure-gradient turbulent boundary layer with nearly constant  $\beta \simeq 1.4$  up to  $Re_\theta \simeq 8700$ . *Journal of Fluid Mechanics* **939**, A34.
- RAHGOZAR, S & MACIEL, Y 2012 Statistical analysis of low-and high-speed large-scale structures

- in the outer region of an adverse pressure gradient turbulent boundary layer. *Journal of Turbulence* (13), N46.
- ROMERO, SYLVIA, ZIMMERMAN, SPENCER, PHILIP, JIMMY, WHITE, CHRISTOPHER & KLEWICKI, JOSEPH 2022 Properties of the inertial sublayer in adverse pressure-gradient turbulent boundary layers. *Journal of Fluid Mechanics* **937**.
- SAMIE, M., MARUSIC, I., HUTCHINS, N., FU, M. K., FAN, Y., HULTMARK, M. & SMITS, A. J. 2018 Fully resolved measurements of turbulent boundary layer flows up to  $Re_\tau = 20\,000$ . *Journal of Fluid Mechanics* **851**, 391–415.
- SANMIGUEL VILA, CARLOS, ÖRLÜ, RAMIS, VINUESA, RICARDO, SCHLATTER, PHILIPP, IANIRO, ANDREA & DISCETTI, STEFANO 2017 Adverse-pressure-gradient effects on turbulent boundary layers: statistics and flow-field organization. *Flow, turbulence and combustion* **99** (3), 589–612.
- SANMIGUEL VILA, CARLOS, VINUESA, RICARDO, DISCETTI, STEFANO, IANIRO, ANDREA, SCHLATTER, PHILIPP & ÖRLÜ, RAMIS 2020 Separating adverse-pressure-gradient and reynolds-number effects in turbulent boundary layers. *Physical Review Fluids* **5** (6), 064609.
- SATO, MAKOTO, ASADA, KENGO, NONOMURA, TAKU, KAWAI, SOSHI & FUJII, KOZO 2017 Large-eddy simulation of naca 0015 airfoil flow at reynolds number of  $1.6 \times 10^6$ . *AIAA journal* **55** (2), 673–679.
- SAVITZKY, ABRAHAM. & GOLAY, M. J. E. 1964 Smoothing and differentiation of data by simplified least squares procedures. *Analytical Chemistry* **36** (8), 1627–1639.
- SILLERO, J. A., JIMÉNEZ, J. & MOSER, R. D. 2013 One-point statistics for turbulent wall-bounded flows at Reynolds numbers up to  $\delta^+ \approx 2000$ . *Physics of Fluids* **25** (10), 105102.
- SKOTE, MARTIN & HENNINGSON, DAN S 2002 Direct numerical simulation of a separated turbulent boundary layer. *Journal of Fluid Mechanics* **471**, 107–136.
- SMITS, A. & MARUSIC, I. 2013 Wall-bounded turbulence. *Phys. Today* **66**(9), 25.
- SMITS, ALEXANDER J, MCKEON, BEVERLEY J & MARUSIC, IVAN 2011 High-reynolds number wall turbulence. *Annual Review of Fluid Mechanics* **43**, 353–375.
- SPALART, P. R. 1988 Direct simulation of a turbulent boundary layer up to  $Re_\theta = 1410$ . *Journal of Fluid Mechanics* **187**, 61–98.
- SPALART, PHILIPPE R. & LEONARD, ANTHONY 1987 Direct numerical simulation of equilibrium turbulent boundary layers. In *Turbulent Shear Flows 5* (ed. Franz Durst, Brian E. Launder, John L. Lumley, Frank W. Schmidt & James H. Whitelaw), pp. 234–252. Berlin, Heidelberg: Springer Berlin Heidelberg.
- SPALART, P. R., MOSER, R. D. & ROGERS, M. M. 1991 Spectral methods for the Navier-Stokes equations with one infinite and two periodic directions. *Journal of Computational Physics* **96**, 297–324.
- SPALART, PHILIPPE R & WATMUFF, JONATHAN H 1993 Experimental and numerical study of a turbulent boundary layer with pressure gradients. *Journal of fluid Mechanics* **249**, 337–371.
- TANARRO, Á, VINUESA, RICARDO & SCHLATTER, PHILIPP 2020 Effect of adverse pressure gradients on turbulent wing boundary layers. *Journal of Fluid Mechanics* **883**.
- TOPALIAN, V., OLIVER, T. A., ULERICH, R. & MOSER, R. D. 2017 Temporal slow-growth formulation for direct numerical simulation of compressible wall-bounded flows. *Physical Review Fluids* **2** (8), 084602.
- WANG, LIMIN, HU, RUIFENG & ZHENG, XIAOJING 2021 A scaling improved inner-outer decomposition of near-wall turbulent motions. *Physics of Fluids* **33** (4), 045120.
- YANG, X. I. A., ZAFAR, S., WANG, J.-X. & XIAO, H. 2019 Predictive large-eddy-simulation wall modeling via physics-informed neural networks. *Phys. Rev. Fluids* **4**, 034602.
- YOON, MIN, HWANG, JINYUL & SUNG, HYUNG JIN 2018 Contribution of large-scale motions to the skin friction in a moderate adverse pressure gradient turbulent boundary layer. *Journal of Fluid Mechanics* **848**, 288–311.
- ZHANG, CHI & CHERNYSHENKO, SERGEI I 2016 Quasisteady quasihomogeneous description of the scale interactions in near-wall turbulence. *Physical Review Fluids* **1** (1), 014401.